RESEARCH ARTICLE

Key Points:

- Lunar metallic ion fluxes vary based on the Moon's location in its orbit but are not heavily reliant on solar activity
- Contributions of heavy ion outflow ($M > 16$ amu) from the Moon could be comparable to those of the ionosphere in the terrestrial environment
- Ion and electron fluxes observed by THEMIS-ARTEMIS are used to calculate sputtering rates, ionization rates, and lunar pickup ion fluxes

Author Contributions:
Conceptualization: Mei-Yun Lin, Andrew R. Poppe
Data curation: Mei-Yun Lin
Formal analysis: Mei-Yun Lin
Funding acquisition: Mei-Yun Lin, Andrew R. Poppe
Investigation: Mei-Yun Lin
Methodology: Mei-Yun Lin, Andrew R. Poppe
Project administration: Andrew R. Poppe
Software: Mei-Yun Lin, Andrew R. Poppe
Supervision: Andrew R. Poppe
Validation: Mei-Yun Lin, Andrew R. Poppe
Visualization: Mei-Yun Lin
Writing – original draft: Mei-Yun Lin
Writing – review & editing: Andrew R. Poppe

Metallic Ions Near the Moon: Impact of Solar Activity and Lunar Position

Mei-Yun Lin[1,2] and **Andrew R. Poppe[1]**

[1]Space Sciences Laboratory, University of California, Berkeley, CA, USA, [2]University Corporation for Atmospheric Research, Boulder, CO, USA

Abstract Metallic ions are commonly found in the cis-lunar environment, primarily produced through the neutral lunar exosphere. They become prevalent species of lunar pickup ions as the Moon moves through the solar wind upstream, magnetosheath, and magnetotail. Extensive studies on the composition of lunar pickup ions from the Lunar Atmosphere and Dust Environment Explorer and THEMIS-ARTEMIS missions have revealed the significant presence of ions with around 28 and 40 amu near the Moon, which are later identified as metallic species such as Al^+, Si^+ and K^+ ions. However, while these studies have provided valuable insights, the abundance of metallic ions and their variations with the Moon's location and solar activity has yet to be understood. This study calculates the production and ionization rates of metallic ions based on in-situ THEMIS-ARTEMIS observations. Our analysis indicates that the magnetosphere effectively reduces the production of metallic neutrals and ions due to the reduction of ionization and sputtering rates. The statistical analysis of the 12-year data set further shows that the lunar pickup ion fluxes are not heavily reliant on solar activity, and the median values remain relatively consistent over time. Therefore, the source rates of metallic pickup ions are associated with the location of the Moon rather than being dependent on solar activity. The outflow rates of heavy ion species from the Moon are comparable with the molecular and metallic ion rates from Earth's ionosphere, suggesting their essential roles in the dynamics of heavy ions in Earth's terrestrial environment.

1. Introduction

While Earth's atmosphere and magnetic field protect the direct access of solar and cosmic particle radiation, the Moon, on the contrary, has a thin atmosphere and no global magnetic field, allowing the impacting particles to modify its surface regolith directly. The collection of these processes is known as space weathering, which plays a critical role in shaping the lunar surface (Denevi et al., 2023; Hapke, 2001; Hunten & Sprague, 1997; Killen & Ip, 1999; Pieters & Noble, 2016). For example, the Moon is constantly exposed to meteoroid impacts excavating the uppermost layers of its regolith (Hunten et al., 1998; Janches et al., 2021). During two-thirds of its 29-day orbit around the Earth, the Moon is exposed to the interplanetary space, allowing the solar wind particles to strike the lunar surface regolith (Hapke et al., 1970; Holmström et al., 2012; Poppe et al., 2017; Tucker et al., 2019). This area is commonly known as the solar wind upstream, which corresponds to the upstream region of Earth's bow shock in the solar wind plasma. For the other one-third of its orbit, the Moon passes through the magnetosheath, lobe-like, and sheet-like plasma. Therefore, the lunar-origin plasma experiences additional particle acceleration in the magnetotail (Cao et al., 2020; Halekas et al., 2018; Kallio & Facskó, 2015; Liuzzo et al., 2022).

These space weathering processes help the Moon sustain a tenuous surface-bounded neutral atmosphere, the so-called lunar exosphere (Hodges et al., 1974; Stern, 1999; Wurz et al., 2022). The lunar exosphere was measured in situ from the Lunar Atmospheric Composition Experiment (LACE) of Apollo 17 (J. Hoffman et al., 1973; R. Hodges Jr et al., 1973) and the Neutral Mass Spectrometer (NMS) of the Lunar Atmosphere and Dust Environment Explorer (LADEE) (Benna et al., 2015; Mahaffy et al., 2015). The optical remote-sensing technique using ground-based measurements was also utilized to detect exospheric Na and K species to understand better lunar exosphere dynamics (Baumgardner et al., 2021; Kagitani et al., 2010; Potter & Morgan, 1998; Wilson et al., 2003, 2006). Some noble gases in the exosphere originate from the lunar interior, such as ^{40}Ar, a product of radiogenic decay of ^{40}K from the lunar crust (Benna et al., 2015; Killen, 2002). Most of the production processes are sourced from the impacting particles, including the sputtering via particles from the solar wind or terrestrial magnetosphere (Poppe et al., 2022; Szabo et al., 2020; Wurz et al., 2007), the neutralization of solar wind particles (Grava et al., 2020; Hurley et al., 2017; Stern et al., 2013), photon-stimulated desorption (PSD) (Gamborino & Wurz, 2018; B. Yakshinskiy & Madey, 1999, B. V. Yakshinskiy & Madey, 2004), and micrometeoroid impact

vaporization (MIV) of the lunar regolith (Barghouty et al., 2011; Nie et al., 2024; Szalay et al., 2016; Verani et al., 1998). In addition to the production mechanisms, the lunar exosphere is removed via surface trapping (Hendrix et al., 2019; R. R. Hodges Jr, 1980; Schorghofer et al., 2021), and gravitational escape for neutrals that with sufficient escape energy. Furthermore, they could undergo ionization processes, such as photoionization, electron impact (EI), and charge exchange with protons, and become so-called lunar pickup ions (Manka & Michel, 1973).

Many species in the lunar exosphere undergo multiple production and loss mechanisms at the same time. These processes are sensitive not only to the impacting particles on the lunar surface but also to the background environment in which the Moon is situated. For example, a tenuous lunar ionosphere was observed to persist even when the Moon traverses the magnetotail, with its ambient density capable of locally perturbing the magnetotail environment (Halekas et al., 2018). Additionally, the neutral densities of the lunar exosphere generated by solar wind sputtering were found to increase by an order of magnitude during the passage of a coronal mass ejection (CME) (Killen et al., 2012). One useful way to investigate the lunar exosphere dynamics is through the detection of lunar pickup ions (PUIs), which primarily originate from the lunar exosphere and ionosphere. This is particularly important for those heavy-mass species that are gravitationally bound. Since heavy-mass species are difficult to remove from the lunar exosphere through gravitational escape, their escape pathways are to become PUIs through ionization processes (photoionization, EI, and charge exchange with protons) and be immediately accelerated by ambient electromagnetic fields from either the solar wind or the magnetotail plasma (Elphic et al., 1991; Hartle & Killen, 2006). Particles that fail to escape via the pick-up process are recycled to the Moon's surface (Poppe, Halekas, Sarantos, & Delory, 2013; Sarantos, Killen, et al., 2012).

Lunar PUIs were first observed in situ by several lunar fly-by spacecraft missions, such as the Ion Release Module (IRM) on the Active Magnetospheric Particle Tracers Explorer (AMPTE) (Hilchenbach et al., 1992, 1993), the Suprathermal Ion Spectrometer (STICS) on the WIND (Mall et al., 1998) and the Geotail (Kirsch et al., 1997) missions. Unlike these fly-by missions that only spent brief periods near the Moon, the lunar-centered missions in recent years provide the average properties of the Moon's plasma environment. Lunar PUIs were directly identified by the lunar orbiters SELENE (KAGUYA) (Tanaka et al., 2009; Yokota et al., 2014, 2020) and LADEE (Halekas et al., 2015; Poppe et al., 2016). With the assumption of exospheric composition, information about lunar PUIs can also be indirectly derived from the energy spectrum observed by Chang'E−1 (Wang et al., 2011) and the Acceleration, Reconnection, Turbulence, and Electrodynamics of the Moon's Interaction with the Sun (ARTEMIS) missions (Halekas et al., 2012, 2016, 2018; Poppe et al., 2012; Poppe, Halekas, Samad, et al., 2013; Shen et al., 2024; Zhou et al., 2013). The composition of lunar PUIs include H_2^+, He^+, C^+, mass 16 (O^+ and CH_4^+), Ne^+, Na^+, Al^+, mass 28 (Si^+ and CO^+), K^+ and $^{40}Ar^+$. The highest count rates of PUIs were typically ions with masses near 28 (Al^+, Si^+, and CO^+) and 40 (K^+ and $^{40}Ar^+$) (Halekas et al., 2012, 2015; Hilchenbach et al., 1993; Mall et al., 1998; Poppe et al., 2012, 2016; Sarantos, Hartle, et al., 2012; Zhou et al., 2013). These findings highlight the significant roles of metallic ions such as Na^+, Al^+, Si^+, and K^+ in the lunar PUIs. However, very few studies have been conducted to constrain the fluxes of these metallic pickup ions. The variations of the lunar exosphere due to PUI escape along the lunar orbit have not yet been fully understood.

The study of lunar metallic ion fluxes not only helps understand the impact of space weathering processes on the lunar regolith but also helps interpret the observations of heavy ions in the terrestrial environment. Ions with mass 28 and mass 56 (Fe^+) have been observed by Geotail to have an extensive range of densities throughout the magnetosheath and inner magnetosphere. Their abundances were also found to correlate with geomagnetic activity (Christon et al., 2017). Si and Fe ions, including those with higher-charge states, were also reported by the Cluster RAPID but indicated no direct correlation between the Kp index and metal ion abundances (Haaland et al., 2021). The contradiction between Geotail and Cluster studies is likely attributed to instrument limitations, as many instruments struggle to differentiate between species, especially those with mass ranges similar to molecular ions. Additionally, since lunar pickup ions are dominated by species with masses close to 28 and 40 amu, these observations suggest that lunar pickup ions may be transported from the Moon to the terrestrial environment, as indicated by previous observations of lunar pickup ions (Halekas et al., 2011; Kirsch et al., 1997). However, the knowledge regarding the sources, convection, and energization of metallic ions, as well as their dynamics in the magnetosphere, has yet to be well understood.

Unlike the pickup ion studies (Poppe et al., 2022; Sarantos, Hartle, et al., 2012) that primarily examine the spatial variations of lunar pickup ions over the lunar surface, this study focuses on evaluating the metallic ion fluxes
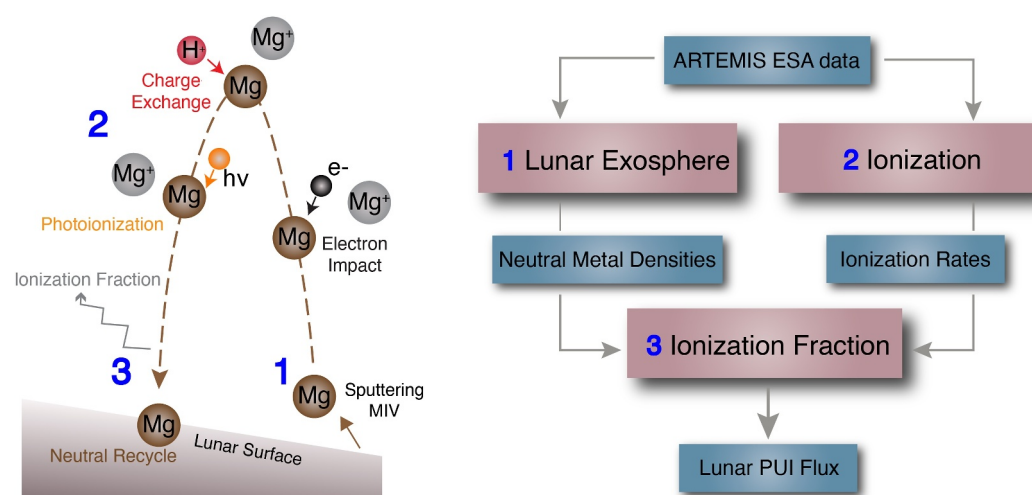
Figure 1. Description of metallic pickup ions from the production to ionization processes. As illustrated in the left figure, the lunar exosphere, once generated, experiences ionization processes. Ions that are not ionized are reimplanted back onto the lunar surface. The right figure presents a diagram outlining the methodology used to derive these metallic pickup ions. In the diagram, blue boxes represent the inputs and outputs of each process, while red boxes indicate the processes corresponding to Section 2.2 through Section 2.4.

originating from the Moon that potentially contribute to Earth's magnetosphere. It will provide context to interpret data from the planned Heliophysics Environmental and Radiation Measurement Experiment Suite (HERMES) on the Lunar Gateway, which has an ion mass spectrometer to distinguish the heavy ions in the cis-lunar environment. Furthermore, the study provides a detailed analysis of ionization rates and metallic pickup ion fluxes based on observational data from the THEMIS-ARTEMIS missions, which could serve as a valuable reference for future lunar models. Since there is no ion mass spectrometer on board ARTEMIS, information regarding the lunar exosphere and the production rates of pickup ions for metallic ions is derived from the incoming electron and ion energy fluxes observed by ARTEMIS. Section 2 outlines the approach taken to develop a metallic pickup ion model based on ARTEMIS data. Section 3 presents two case studies that illustrate conditions during Solar Maximum and Minimum periods. Section 4 provides statistical analyses of ionization rates and fluxes based on a 12-year data set from ARTEMIS. Finally, Section 5 estimates the escape of ions from Earth's ionosphere and the Moon for various species and discusses the implications of these comparisons for terrestrial observational data.

2. Methodology

This study evaluated the lunar PUI fluxes by considering the production and ionization processes for metallic Na^+, Mg^+, Al^+, Si^+, K^+, Ca^+, Ti^+, and Fe^+ ions, based on the similar scope of the PUI model developed by Poppe et al. (2022). As shown in Figure 1 left panel, the impact of incoming charged particles and micrometeoroids on the lunar surface produces neutral metals (step 1 process). These neutrals then perform ballistic travel while, at the same time, undergoing ionization processes through EI, charge exchange with protons (CX), and photoionization (PHI) processes and become the lunar PUIs (step 2 process). The produced neutral metals that are ionized within the ballistic trip become the PUIs and may escape from the lunar surface (step 3 process). This study, illustrated in Figure 1 right panel, utilizes the observed ion and electron energy fluxes to derive the neutral metal densities and ionization rates of metallic ions in the lunar exosphere, shown in Sections 2.2 and 2.3. The derived information on neutral production and ionization rates is further used to obtain the ionization fraction (Section 2.4), which indicates the possibility of produced neutrals becoming ions to escape before they are recycled to the surface.

2.1. THEMIS-ARTEMIS Observations

Originally part of the Time History of Events and Macroscale Interactions during Substorms (THEMIS) mission, the THEMIS-ARTEMIS mission (referred to as ARTEMIS mission in this paper) consists of two identical probes, namely ARTEMIS-P1 and P2, with ion and electron Electrostatic Analyzers (McFadden et al., 2008) and electric and magnetic field measurements (EFI and FGM) (Auster et al., 2008; Bonnell et al., 2009). Both probes are in
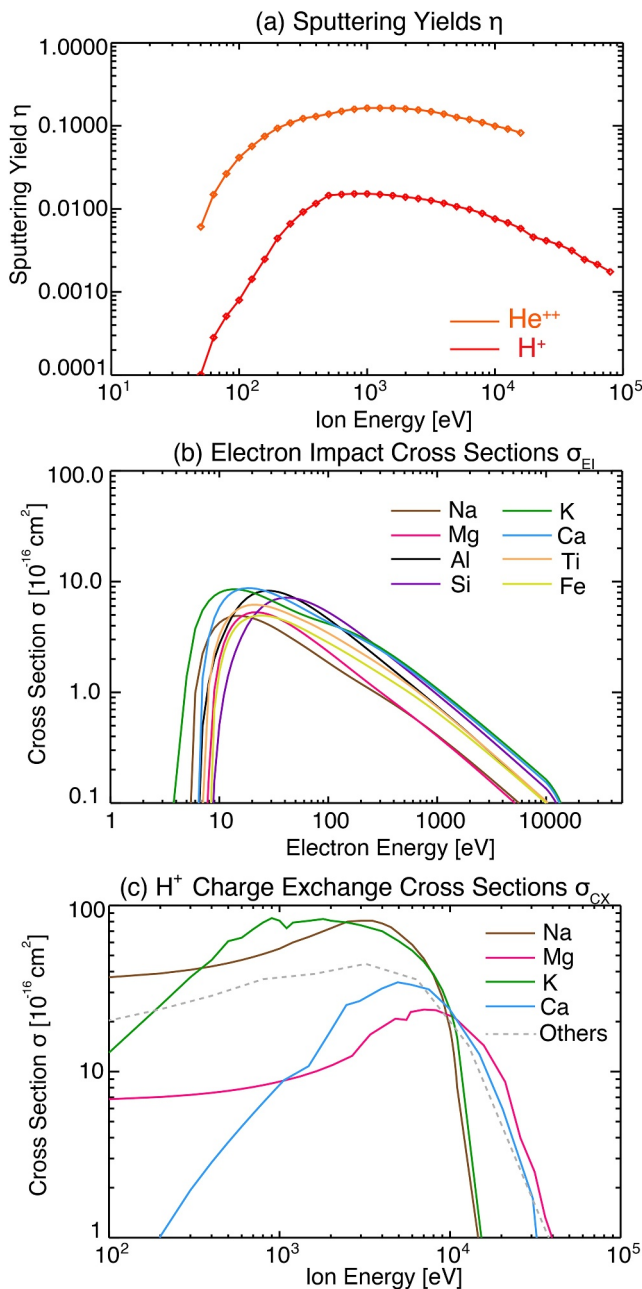
Figure 2. (a) Sputtering yields rate versus ion energy for H$^+$ (red dotted line) and He^{++} (orange dotted line), extracted from Figure 17 in the study of Biersack and Eckstein (1984); (b) electron impact cross-section area (in the unit of 10^{-16} cm^2) versus incoming electron energy for neutral Na (brown), Mg (magenta), Al (black), Si (purple), K (green), Ca (light blue), Ti (orange) and Fe (gray); (c) cross-section area (in the unit of 10^{-16} cm^2) of charge exchange with protons versus incoming proton energy for neutral Na (brown), Mg (magenta), K (green), Ca (light blue), and other species (gray).

highly elliptical, near-equatorial, and asynchronous orbits around the Moon with periselenes between 10 and 1,000 km and aposelene of 20,000 km (10 lunar radii), with periods of approximately 24–26 hr (Angelopoulos, 2010). The particle moment calculations take into account spacecraft charging corrections for angle and energy measurements, with spacecraft potential values measured by the ARTEMIS Electric Field Instrument (Bonnell et al., 2009; McFadden et al., 2008). Unfortunately, no ion mass spectrometer is available on ARTEMIS. Therefore, the information on pickup ion species requires indirect derivation from the ARTEMIS observations with a modeling approach. To exclude the influence of lunar interactions, measured data that is too close to the Moon (<2 R_L) or inside the lunar wake region are not considered in the following calculations. ESA data are snapshots of the plasma with a measurement cadence of either 32 spins (in "Fast-Survey Spacecraft-Mode", approximately every 2 min) or 128 spins ("Slow-Survey Spacecraft-Mode", every 8 min) (McFadden et al., 2008). To minimize the measurement influence due to operation, the data observed during the transitions between fast and slow modes are also not considered.

2.2. Neutral Production Rate

When incoming particles collide with the lunar regolith, they can release elements from the lunar soil. The production mechanisms of neutral metals are categorized based on the source of these particles, including neutral sputtering, MIV, and PSD. MIV occurs when micrometeoroids strike the lunar surface, leading to the vaporization of material, and its neutral production rate is constrained by the LADEE observational data. The lunar surface is vaporized by MIV at an average mass flux R_{MIV} of 1.16×10^{-15} (g cm^{-2} s^{-1}) (Pokorný et al., 2019). To accurately calculate the neutral production rates for metallic ion species, compositional estimates of the lunar surface are necessary. These estimates are derived from samples collected from four distinct types of lunar soils—Highland, KREEP, low-Ti, and high-Ti Mare soils—along with the masses and percentages of metallic neutral species (Heiken et al., 1991; Papike et al., 1982; Wurz et al., 2007). This study assumes an average composition of metallic species with the following percentages (C): C_{Na} (0.29%), C_{Mg} (3.84%), C_{Al} (10.66%), C_{Si} (16.31%), C_K (0.05%), C_{Ca} (5.92%), C_{Ti} (0.17%), and C_{Fe} (1.9%). In addition, PSD involves the desorption of neutrals from the lunar regolith as a result of solar photon absorption, a process known to be particularly efficient for sodium (Na) and potassium (K) (B. Yakshinskiy & Madey, 1999; B. V. Yakshinskiy & Madey, 2004). However, this mechanism is not included in the scope of this study as it would require a full three-dimensional Monte Carlo model of Na and K dynamics that includes the prominent effect of solar radiation pressure (e.g., Smyth & Marconi, 1995; Tenishev et al., 2013). Thus, the Na$^+$ and K$^+$ ion escape rates calculated here with only sputtering and MIV contributions should be regarded as a lower limit.

Charged particle sputtering is often regarded as a significant source of refractory elements found in the lunar exosphere. When charged particles from the solar wind or magnetospheric plasma collide with the lunar surface, they can eject neutrals from the regolith. Incoming solar wind particles, including protons (H$^+$) and alpha particles (He^{++}), are particularly effective at sputtering these neutrals, with alpha to proton density ratios typically centered around a few percent (Kasper et al., 2007). As illustrated in Figure 2a, the sputtering yield rates depend on incoming species (Biersack & Eckstein, 1984). The sputtering yield rates of He^{++} are larger than those of H$^+$ by an order of magnitude, both peak at ~1 keV. Therefore, this study derives the

densities and velocities of incoming H^+ and He^{++}, respectively, to the lunar surface from the ion energy spectra measured by ARTEMIS.

Since no ion mass spectrometer is available on ARTEMIS mission, this is achieved by fitting two convecting Maxwellian distributions, as developed by Halekas et al. (2014), Benna et al. (2015). The fitting approach modifies the parameters of Maxwellian distributions for protons and alpha particles to minimize the chi-square error, allowing for a better fit to the observed ESA energy flux spectrum. Once the optimal parameters are determined, they are converted back into the velocity and number density of H^+ and He^{++}. This approach is only valid where the energy flux peak of H^+ and He^{++} can be distinguished, typically the solar wind region where the Mach number is high. However, this fitting approach is no longer valid when the Moon crosses the magnetosphere, including magnetosheath and magnetotail regions, which have a low Mach number. Instead, a relatively simple assumption is applied that He^{++} densities is ~3% of total plasma density, and the velocity of He^{++} and H^+ are assumed to be equal. Figure 3a illustrates an example of separating H^+ and He^{++} from the ARTEMIS energy flux spectrum observed on 11 September 2023. The two Maxwellian distributions represent the distinct energy profiles of H^+ (orange curve) and He^{++} (red curve), with the fitted distribution functions centered at 650 and 1210 eV, respectively. Notably, the discrepancies between the fitted functions and the observational data are all within 1%.

With the aforementioned information, the sputtering rate $R_{sputtering}$ is calculated by integrating the energy flux curves $\Phi(E)$, which are the curves for He^{++} and H^+ depicted in Figure 3a, alongside the yield rate profiles $\eta(E)$ shown in Figure 2a: $R_{sputtering} = \int_E \Phi(E)\eta(E)dE$ (cm^{-2}s^{-1}). Additionally, to determine the neutral production rate P per species (cm^{-2}s^{-1}), the sputtering rate $R_{sputtering}$ is combined with the previously discussed MIV rate R_{MIV}, multiplying the soil composition of the lunar surface C for each metallic species. For instance, the production rate for Mg is expressed as $P_{Mg} = (R_{sputtering} + R_{MIV})C_{Mg}$.

2.3. Ionization Rate

Once metallic neutrals are generated via sputtering or MIV, they undergo various ionization processes to become metallic ions, including photoionization, EI, and charge exchange with protons. Photoionization rates of metallic neutrals (R_{photo}) are directly obtained from the database of photoionization/dissociation rates, which provides the photoionization rates of each neutral metallic species for different solar activity levels (W. F. Huebner & Carpenter, 1979; W. F. Huebner et al., 1992; W. Huebner & Mukherjee, 2015). Since solar activity varies with the photoionization rates, this study evaluates the photoionization rates in relation to sunspot numbers, which serve as a proxy for solar activity. For instance, the photoionization rates of Mg^+ during periods of solar maximum and minimum are measured at 6.07 and 11.7×10^{-7} s^{-1}, respectively. The photoionization rates for other conditions are derived by interpolating these values based on the observed sunspot numbers. For EI (R_{EI}) and charge exchange (R_{CX}) rates, the ion and electron energy flux spectra observed by ARTEMIS are further utilized to derive the proton and electron fluxes that contribute to ionization rates for each metallic species. While the proton fluxes are obtained via the fitting approach in Section 2.2, the electron fluxes are rather straightforward to obtain from the ARTEMIS observations. Figure 2b shows the cross sections versus particle energy on EI processes (Bartlett & Stelbovics, 2002, 2004), and charge exchange with protons processes (Ebel & Salzborn, 1987; Morgan et al., 1985; Rutherford & Vroom, 1972). While EI cross-sections for each metallic ion species are available, the charge exchange processes between protons and neutral metals are not available for all metal species, including Al, Si, and Ti. Therefore, the cross-section for these species is the average cross-section of Na, Mg, K, and Ca, which is indicated as "Others" in Figure 2c. Given various cross-sections for different EI and CX processes, $R_{EI/CX} = \int_E \Phi(E)\sigma(E)dE$ (s^{-1}).

2.4. Ionization Fraction

When neutrals are produced through sputtering or MIV, they travel ballistically while simultaneously undergoing ionization processes. The ionization fraction is defined as the likelihood of neutrals being ionized before reimplanting on the lunar surface. It represents the ratio of neutrals that become ionized and eventually escape to those that are recycled back to the lunar surface. This can be expressed by the following equation:

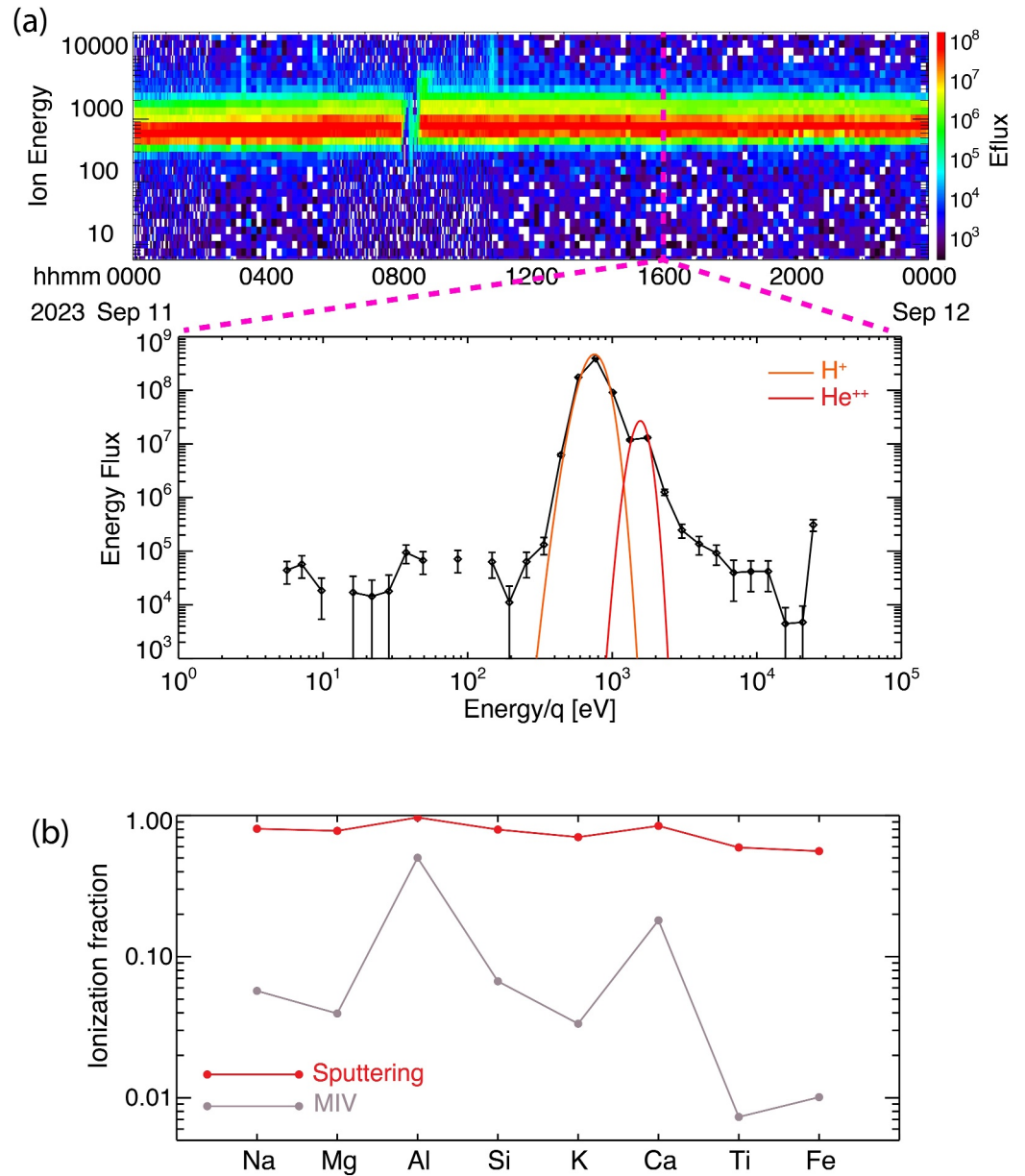$$f_{ionization} = 1.0 - \exp(-T_{flight}/T_{ionized}) \tag{1}$$

Figure 3. (a) Description of fitting the ESA ion energy flux spectrum with two convecting Maxwellian distributions to obtain the densities and velocities of H^+ and He^{++}. The error bar is the counting error of ARTEMIS ESA measurement; (b) Ionization fraction for neutral metals that are produced from sputtering (red dotted line) and micrometeoroid impact vaporization (gray dotted line).

where T_{flight} is the ballistic flight time for neutrals, which depends on the velocity distribution of the produced neutrals and their mass. $T_{ionized}$ is the time for neutrals to be ionized and can be approximated as the $\frac{1}{R_{photo} + R_{EI} + R_{CX}}$, where R_{photo}, R_{EI}, and R_{CX} are the ionization rates of photoionization, EI, and charge exchange with protons for each metallic species. With the information on ionization fraction $f_{ionization}$, the derived lunar PUI flux Φ_{sp} ($cm^{-2}s^{-1}$) for each metallic species $\Phi_{sp} = P_{sp} f_{ionization,sp}$, where subscript sp is referred to as metallic species.

The velocity distributions used to calculate the ballistic flight time vary depending on the production mechanisms of the neutrals from sputtering or MIV. The velocity distributions from neutral sputtering follow a Sigmund–Thompson energy distribution (referred to as S-T distribution afterward), which has a more extended tail at higher energies (Sigmund, 1969; Thompson, 1968). On the other hand, the velocity distributions from neutrals

produced via MIV are closer to a thermal distribution (Collette et al., 2013; Eichhorn, 1976, 1978). Figure 3b shows an example of the ionization fraction due to sputtering and MIV based on the ARTEMIS data observed on 11 Sep. 2023, which its energy flux spectrum, H^+ and He^{++} energy distribution are described in Figure 3a. The more energetic velocity distribution functions for sputtering lead to sputtered neutrals having higher velocities and longer ballistic flight times compared to those from MIV. As a result, the ionization fractions for sputtering approaches unity, indicating that most sputtered neutrals are ionized and escape from the lunar exosphere. In contrast, only 1%–10% of neutrals produced from MIV are ionized and converted into pickup ions. Furthermore, the ionization fraction rate varies among different species. Al has the highest ionization fraction among the eight metallic species since its total ionization rate is $\sim 1.25 \times 10^{-3} \text{ s}^{-1}$, while others' ionization rates are on the order of 10^{-6}–10^{-5} s^{-1}. It is important to note that ionization rates fluctuate over time, as the rates for EI and CX rates depend on the incoming electron and proton fluxes measured by the ARTEMIS spacecrafts.

3. Case Studies

This section focuses on case studies examining the production of lunar pickup ion fluxes from the lunar exosphere, utilizing observational data from the ARTEMIS mission during a single lunar orbit around the Earth. Two complete lunar orbits are analyzed to compare the effects of solar activity: one is during a typical solar maximum, while the other occurs during a solar minimum. Throughout these two time periods, the Moon moved from the solar wind upstream region to the magnetosheath, lobe, and plasma sheet, left the magnetosphere region, and emerged back into the solar wind upstream region. Although all metallic ions originating from the Moon have various abundances, they exhibit similar behaviors. Therefore, Mg^+ (with a mass ~ 24 amu) has been selected as the representative metallic ion for this study.

3.1. Case Study: Solar Maximum

Figures 4a and 4b are the observed total electron and ion fluxes from the ARTEMIS-P1 observational data of a complete lunar orbit from Aug. 15th to 15 Sep. 2023. The space weather in this lunar orbit is mostly quiet, except for a moderate geomagnetic storm (min Dst $\sim$ -80 nT) on Sep 12th. Both figures show that the Moon passed through the magnetosphere, including magnetosheath (highlighted as yellow regions), lobe, and plasma sheet, from Aug 27th to Sep 3rd. This period is identified by characteristic changes in both the ion and electron fluxes from the ESA measurement. With the fitting technique introduced in Section 2.2, the fluxes of H^+ and He^{++} from Figure 4a are derived and shown in Figure 4c. The gray region from (c) to (g) indicates the region where He^{++} densities are assumed to be 3% of H^+ densities. From Aug 29th to 31st, no significant ion fluxes were observed by the ARTEMIS mission, leading to an absence of sputtering rate profiles during that time. Additionally, as mentioned in Section 2.2, with sputtering yield rates, the derived H^+ and He^{++} fluxes and lunar soil composition, the neutral Mg production rate from sputtering and MIV are obtained; see Figure 4d. The ionization rates of neutral Mg via PHI, EI, and CX are also derived with ionization profiles in Section 2.3. It's important to highlight that the gray region does not fully align with the magnetosheath (yellow regions). This is because the magnetosphere boundary in this study is defined by the condition: $-1 \leq Y_{GSE}/X_{GSE} \leq 1$ and $X_{GSE} \leq 0$, which cannot capture the variations in Earth's magnetosphere boundary.

Figures 4c–4e demonstrate that the magnetosphere serves not only as a shield for Earth's atmosphere but also protects the Moon from the impacts of space weathering. The rate of magnesium (Mg) sputtering is primarily influenced by the incoming fluxes of H^+ and He^{++} ions, meaning that this sputtering rate varies depending on the Moon's position in its orbit. He^{++} densities can reach 10% of H^+ densities when the Moon is in the solar wind region. Since the H^+ and He^{++} fluxes largely decreased by two orders of magnitudes, the Mg sputtering and subsequent ionization rates were also reduced. Additionally, ionization rates are affected by the Moon's location. When the Moon is in the solar wind region, it experiences increased impacts from H^+ and He^{++} ions as well as electrons, resulting in elevated ionization rates from EI and CX. Conversely, when the Moon is within the magnetosphere, the electron and ion fluxes decrease, significantly lowering the EI and CX ionization rates, while photoionization becomes the primary mechanism for ionizing neutral Mg. It is important to note that the production rate of neutral Mg from MIV in our study remains constant. Although MIV production varies according to the lunar location in its orbit (Szalay & Horányi, 2015), these variations are minor enough to be considered negligible.
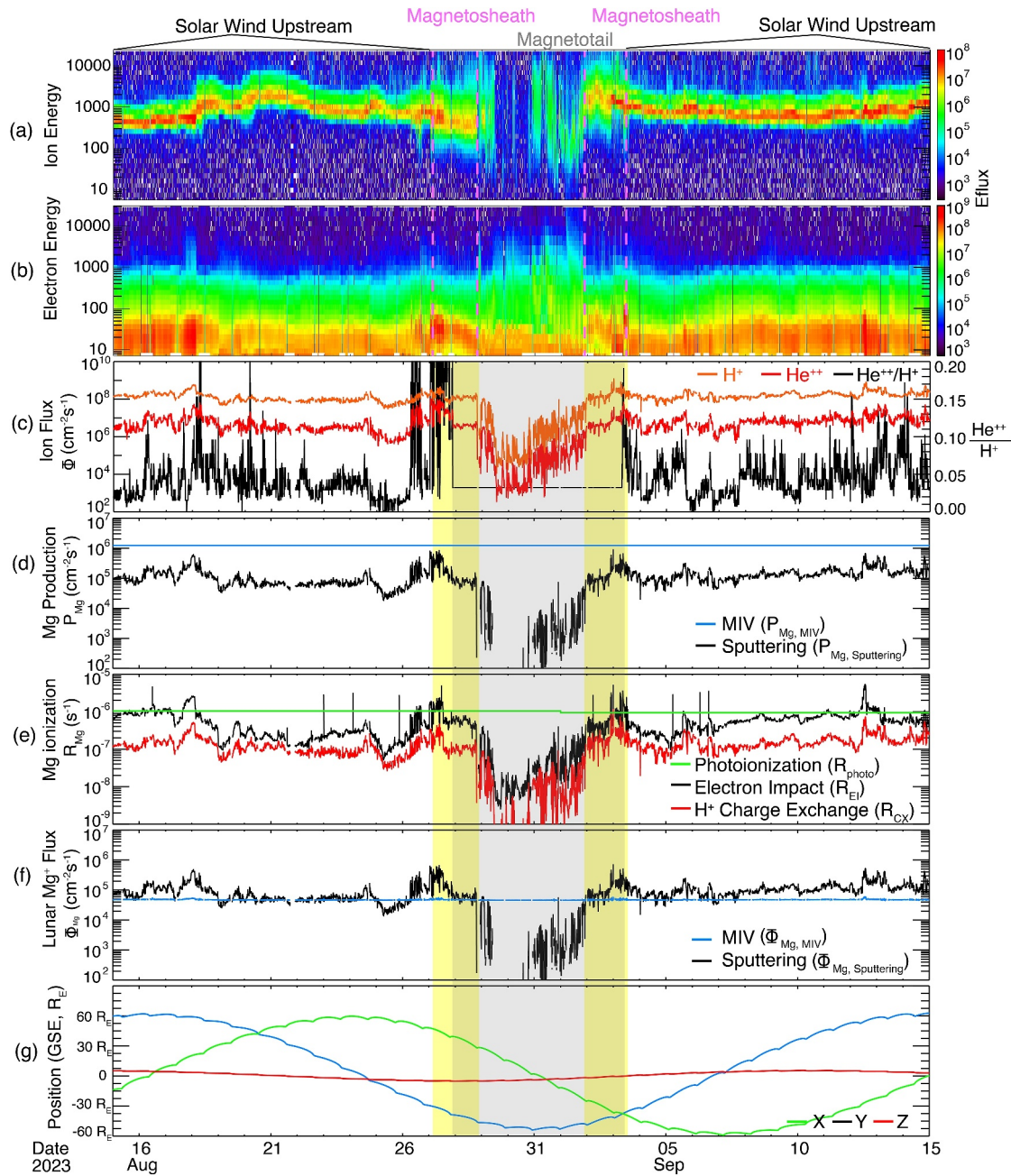
Figure 4. ARTEMIS P1 measurements and derived Mg+ production and ionization rates from Aug. 15th to 15 Sep. 2023, which represents a typical month in Solar Maximum condition: (a) Full ESA ion energy flux; (b) full ESA electron energy flux; (c) H^+ (orange solid line) and He^{++} (red solid line) ion densities by fitting the ESA ion energy flux (a); (d) production rates of neutral Mg through sputtering (black solid line) and micrometeoroid impact vaporization (MIV) (light blue solid line); (e) Ionization rates of neutral Mg through the photoionization (green line), electron impact (black line), and charge exchange with protons (red line); (f) lunar Mg^+ pickup fluxes produced via neutral sputtering (black line) and MIV (light blue line); (g) ARTEMIS position in GSE coordinates in unit of R_E. ESA Energy fluxes are measured in units of $eV\ cm^{-2}\ s^{-1}\ str^{-1}\ eV^{-1}$. The yellow regions indicate when ARTEMIS traverses the magnetosheath, while the gray region denotes where $n(He^{++})$ are assumed to be 3% of $n(H^+)$.

The resulting ionization rates, together with the neutral Mg production rates, allow us to calculate the ionization fraction of Mg^+ and the subsequent production of Mg^+ lunar pickup ion fluxes, as shown in Figure 4f. As mentioned in Section 2.4, the differing velocity distribution functions of sputtering and MIV lead to most neutral Mg produced via sputtering being ionized and escaping from the lunar surface, while approximately 90% of neutral Mg from MIV is recycled back to the surface. Comparing the neutral Mg production in Figure 4d, it is

evident that the lunar Mg$^+$ flux in Figure 4f is primarily driven by sputtering, particularly during geomagnetic storms or when the Moon transitions between the magnetosphere and solar wind regions. However, because the Mg sputtering rates are significantly reduced within the magnetosphere, MIV becomes the dominant mechanism for Mg$^+$ production within the magnetotail.

It is noteworthy that significant fluctuations in ionization rates and fluxes occurred when the Moon was approaching or leaving the magnetosphere. Figure 4 indicates that from Sep. 26th to 28th and Oct. 3rd to 5th, peaks in H$^+$ and He^{++} densities, neutral Mg sputtering rates, and ionization rates all increase by a factor of 3–5. The spikes in H$^+$ and He^{++} densities and the resulting lunar PUI fluxes are attributed to enhanced local plasma fluxes when the solar wind plasma is diverted around the Earth through the magnetosheath (Li et al., 2023; Poppe et al., 2018).

3.2. Case Study: Solar Minimum

Figure 5 presents a case study from Aug. 10 to Sept. 10, 2018, which reflects a typical lunar orbit during solar minimum conditions based on the ARTEMIS-P1 observational data. The space weather during this month was generally quiet. However, on 26 Aug. 2018, there was a geomagnetic storm with a minimum Dst of approximately −180 nT and a maximum Kp of about 7, marking it as the third-largest geomagnetic storm of Solar Cycle 24 (Gopalswamy et al., 2022). During this time, the Moon traversed the magnetosphere region from Aug. 23 to Aug. 31, meaning that it was inside the magnetosphere when the geomagnetic storm impacted the terrestrial environment. As explained in Section 2.1, to exclude the lunar interactions, the data measured in the lunar wake region is not considered in this study. As a result, the gaps in Figure 5 are due to the unavailability of the ESA data. All the derived quantities, from the He^{++} densities of the fitting technique in Section 2.2 to the resulting PUI fluxes, are invalid within these periods.

As shown in Figure 5c, the fluxes of He^{++} are generally only 1%–3% of H$^+$ fluxes during solar minimum, in contrast to 10% or even 30% during solar maximum. Notably, the magnitude of H$^+$ fluxes in the solar minimum is comparable with those during the solar maximum (McComas et al., 2013; Schwenn, 2007). It is important to clarify that the fitting technique is not applied when the Moon is within the magnetosphere, so He^{++} fluxes are assumed to be consistently 3% of H$^+$ fluxes in that region, as discussed in Section 2.2. When comparing Figures 4 and 5, the relative roles of sputtering and MIV, as well as the significance of ionization from PHI, EI and CX, remain similar across both solar maximum and minimum. Given that the incoming H$^+$ fluxes maintain a similar magnitude during solar minimum, the values for the Mg sputtering rate (d), ionization rates (e), and the resulting Mg$^+$ pickup flux (f) during this period are comparable to those derived during solar maximum. This observation suggests that solar activity may not have a significant impact on the average value of lunar pickup ion fluxes.

The geomagnetic storm on 26 Aug. 2018, underscores the importance of magnetospheric shielding for lunar space weathering, particularly in the sub-keV particles. As shown in Figures 5a and 5b, the ion and electron energy fluxes observed from ARTEMIS did not increase significantly while the Moon transited the magnetotail because magnetospheric shielding effectively blocks particles impacting the lunar surface. As a result, the sputtering and ionization rates of Mg did not show a significant increase during this time, and the produced lunar pickup ion fluxes remain relatively stable when the Moon is inside the magnetosphere. This stability also highlights the potential for lunar pickup ions to return to terrestrial environments, as geomagnetic storms can increase plasma velocities in the Earth-Moon region within the magnetotail, facilitating the transport of lunar-origin ions back to the magnetosphere (Halekas et al., 2011; Kirsch et al., 1997; Liuzzo et al., 2022).

4. Statistical Analysis of the 12-Year ARTEMIS Data Set

Figures 4 and 5 indicated that lunar Mg fluxes are reduced when the Moon is inside the magnetosphere compared to times when the Moon is outside the magnetosphere due to a decrease of PUI fluxes via sputtering. This section analyzes the 12-year ARTEMIS data, including both P1 and P2, from the year 2012–2023. The dependence of ionization rates (Section 4.1) and Mg pickup ion fluxes (Section 4.2) on solar activity is further investigated through statistical analysis.
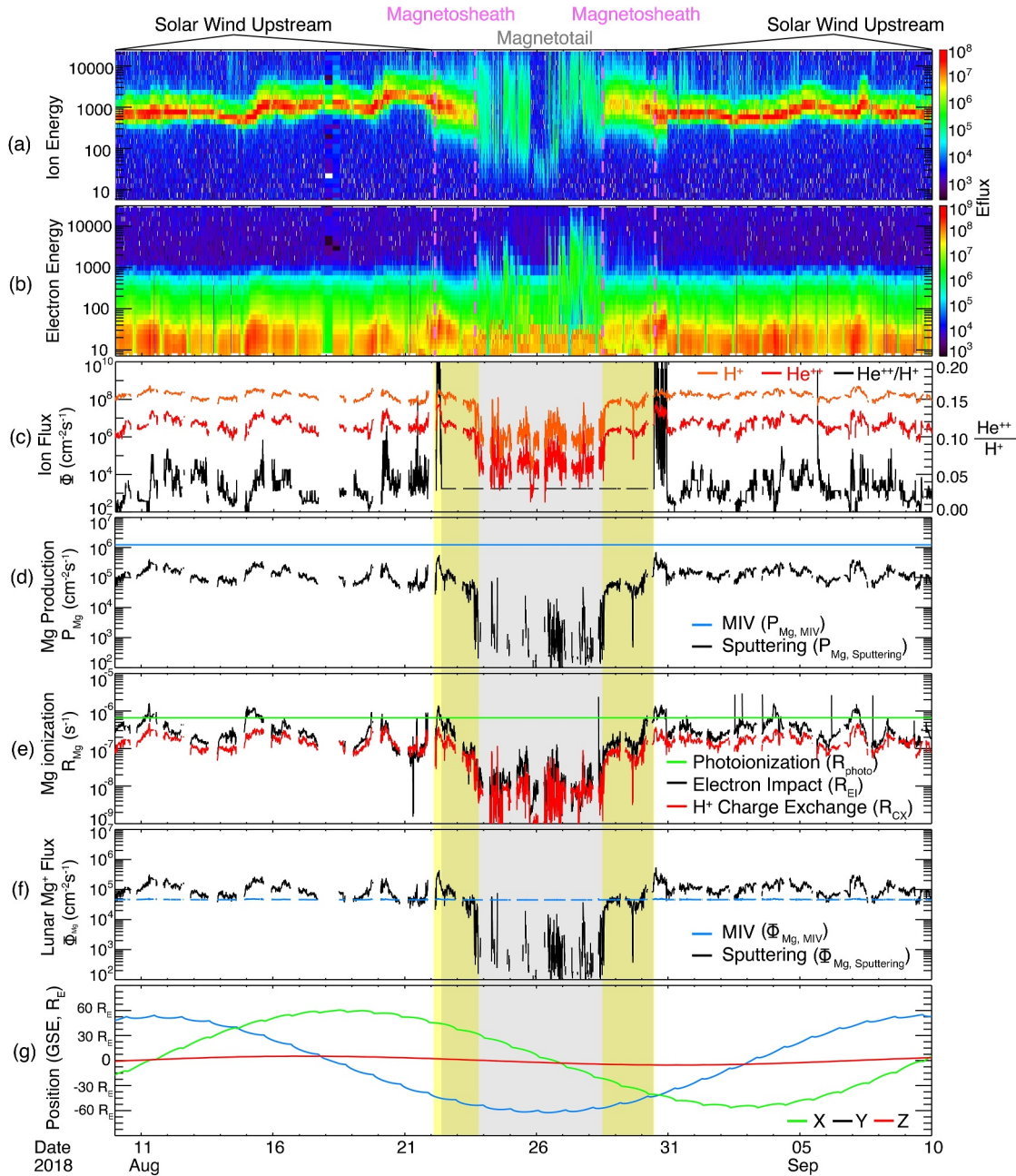
Figure 5. ARTEMIS P1 measurements and derived Mg$^+$ production and ionization rates from Aug. 10th to 10 Sep. 2018, which represents a typical month in Solar Minimum condition: (a) full ESA ion energy flux; (b) full ESA electron energy flux; (c) H$^+$ (orange solid line) and He^{++} (red solid line) ion densities by fitting the ESA ion energy flux (a); (d) production rates of neutral Mg through sputtering (black solid line) and micrometeoroid impact vaporization (MIV) (light blue solid line); (e) Ionization rates of neutral Mg through the photoionization (green line), electron impact (black line), and charge exchange with protons (red line); (f) lunar Mg$^+$ pickup fluxes produced via neutral sputtering (black line) and MIV (light blue line); (g) ARTEMIS position in GSE coordinates in unit of R$_E$. ESA Energy fluxes are measured in units of eV cm^{-2} s^{-1} str^{-1} eV^{-1}. The yellow regions indicate when ARTEMIS traverses the magnetosheath, while the gray region denotes where n(He^{++}) are assumed to be 3% of n(H$^+$).

4.1. Ionization Rates

Figure 6 illustrates the distribution functions of magnesium (Mg) ionization rates for EI and charge exchange (CX) processes from 2012 to 2023. In each panel, the black and orange lines represent yearly distribution functions of the ionization rates from the year 2012–2023, and the red line indicates the average distribution functions for 12-year data. To further investigate how the magnetosphere shields ionization rates, the distribution
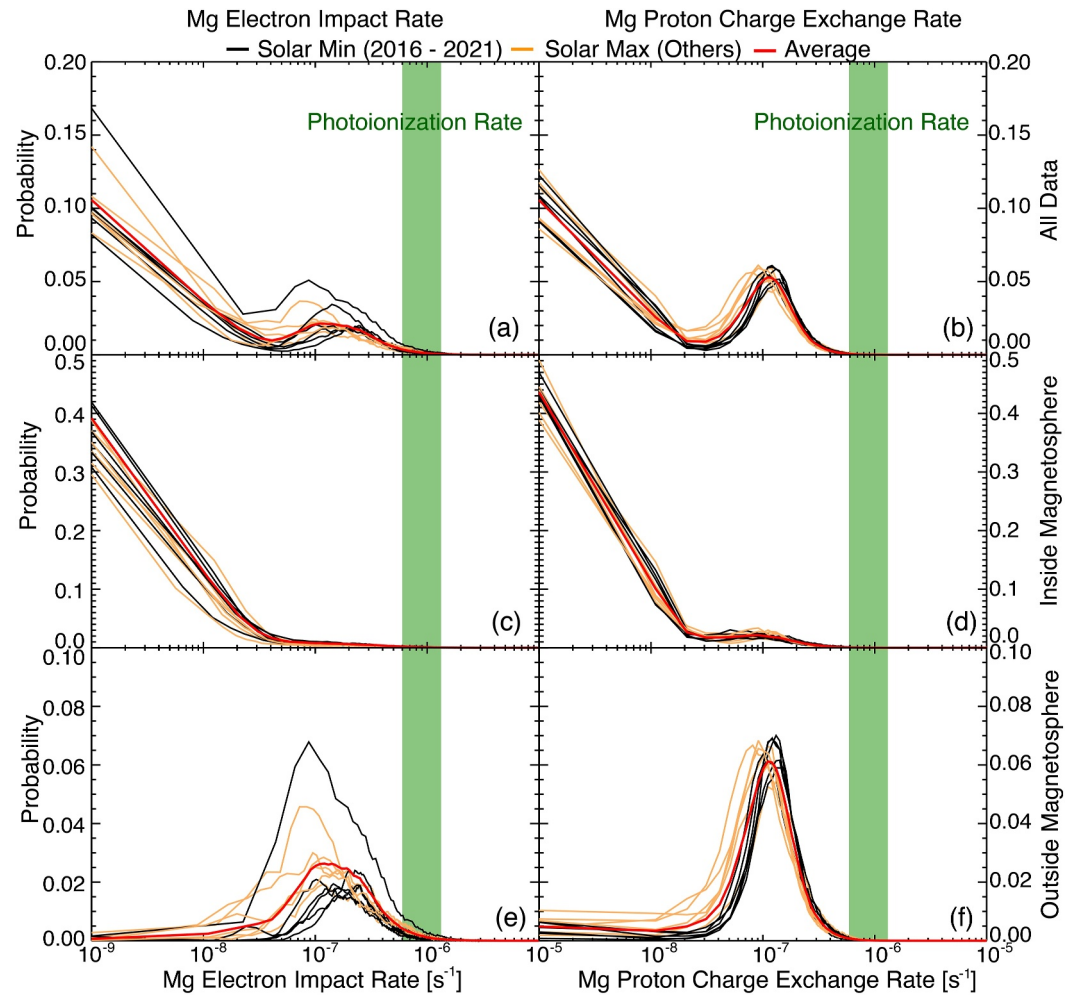
Figure 6. Black and orange lines represent yearly distribution functions of the Mg$^+$ ionization rates from the year 2012–2023, and the red line indicates the average distribution functions for 12-year data. Mg$^+$ ionization rates are categorized by the Moon's location in its orbit, including all data (top row), inside magnetosphere (middle row), and outside magnetosphere (bottom row). Mg$^+$ ions are produced from the ionization of neutral Mg through electron impact (a, c, and e) and charge exchange with a proton (b, d, and f). Ionization rates based on observational data during solar minimum (2016–2021) and maximum (other years) are marked black and orange, respectively. Averaged ionization rates are shown as the red solid line for the total 12 years. The green boxes represent the Mg$^+$ ionization rates via photoionization.

functions are separated into times when the Moon is inside (c, d) and outside (e, f) the magnetosphere. For EI processes (a), the distribution functions predominantly consist of two types: a decay function for rates below 10^{-8} s^{-1} (c) and a Maxwellian distribution for rates between 10^{-8} and 10^{-6} s^{-1} (e). Similarly, the distribution functions for charge exchange (CX) processes (b) also comprise a decay function in (d) and a Maxwellian function in (f). The decay functions for EI and CX rates are derived from ARTEMIS observations when the Moon is within the magnetosphere, while the Maxwellian functions are obtained from measurements taken when the Moon is outside the magnetosphere. This difference in distribution functions indicates that ionization rates are significantly influenced by magnetospheric shielding. When the Moon traverses the magnetosphere, it effectively protects the Moon from solar wind protons and electrons, resulting in a reduction of ionization rates by two orders of magnitude.

The distribution function for the years 2016–2021 is classified as solar minimum (represented by black solid lines in Figure 6), while distributions for the remaining years are labeled as solar maximum (indicated by orange lines). The ionization rates for EI show no clear dependence on solar activity, whereas CX rates are slightly lower during solar maximum compared to solar minimum, particularly when the Moon is outside the magnetosphere. As
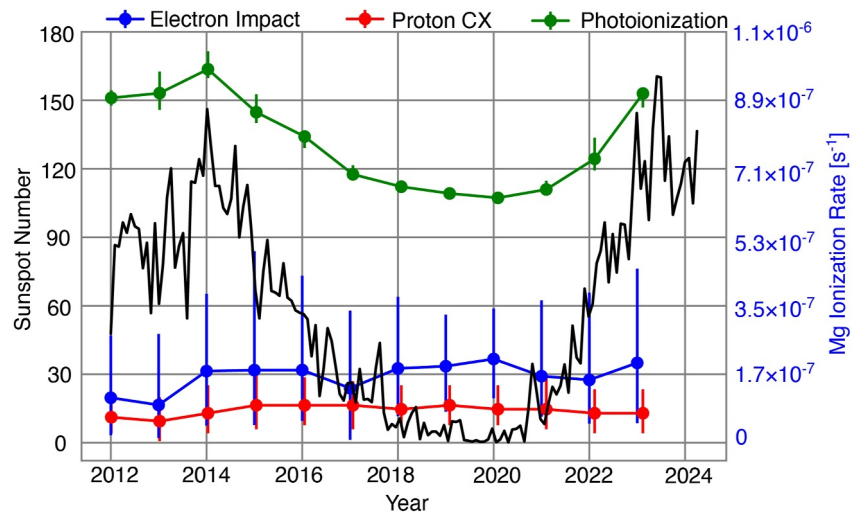
Figure 7. Mg^+ ionization rates versus solar activity between the year 2012 and 2023. Mg^+ ions are produced from the ionization of neutral Mg through electron impact (blue), charge exchange with a proton (red) and photoionization (green). Solar activity is represented by the sunspot numbers (black). Colored points are the median values of Mg^+ ionization rates, and solid lines represent the IQRs.

depicted in Figure 6f, the probability of CX rates falling below 10^{-7} s^{-1} is approximately 50% higher during solar maximum (orange lines) than during solar minimum (black lines). The median CX rates during solar maximum are about 9×10^{-8} s^{-1}, while during solar minimum, they can reach approximately 1.5×10^{-7} s^{-1}. This discrepancy is related to the cross-sectional profiles shown in Figure 2, where the EI cross-sectional area decreases gradually after reaching its peak, and the CX area decreases sharply after a certain proton energy. Since the median ion and electron energy increase during solar maximum, EI rates do not change significantly due to the gradual decline of the EI cross-sectional area, leading to the wide dispersion of R_{EI}. However, increased proton energies during solar maximum results in lower CX rates because of the abrupt reduction in the CX cross-section profile.

Figure 7 illustrates the time variation of ionization rates of Mg through photoionization (green dots and lines), EI (blue dots and lines), and CX processes (red dots and lines) alongside sunspot numbers that indicate solar activity from 2012 to 2023. The interquartile range (IQR) reflects the variability in the data and is defined as the difference between the third quartile (Q_3) and the first quartile (Q_1), specifically $IQR = Q_3 - Q_1$. The colored solid lines in Figure 7 mark the IQR. Generally, the EI rates for neutral Mg are 2–3 times higher than the CX rates, and the IQRs for EI rates are also larger than those for CX rates by the same factor. Notably, the photoionization rates are larger than the EI and CX rates by a factor of ~5. These features are also seen in Figure 6, which shows that the EI distribution functions have higher probabilities at greater values, whereas the distribution functions of CX and photoionization are more centered around the median values. Both the median EI and CX rates are not influenced by solar activity, while median photoionization rates are elevated during solar maxima compared to solar minima. Nevertheless, all the IQRs for photoionization, EI, and CX rates appear to depend on solar activity, with maximum IQRs occurring during solar maxima.

This study provides constraints on the Mg^+ ionization processes and explores variations based on whether the Moon is inside or outside the magnetosphere. According to the lunar pickup ion model by Poppe et al. (2022), the ionization rates of Mg^+ for EI and CX processes are estimated to range from 10^{-8}–10^{-6} s^{-1}. This study further suggests that the ionization rates of Mg^+ for EI and CX processes are mostly likely on the order of 10^{-7} s^{-1} when the Moon is outside the magnetosphere. Additionally, the ionization rates for both EI and CX processes drop below 10^{-8} s^{-1} when the Moon is inside the magnetosphere. It is noteworthy to point out that the photoionization rates of Mg are varied between $6.07 - 11.7 \times 10^{-7}$ s^{-1} in this study, meaning that EI and CX are not as effective as photoionization for ionization processes. Nevertheless, these derived ionization rates will serve as a valuable reference for other lunar exosphere models concerning ionization processes.
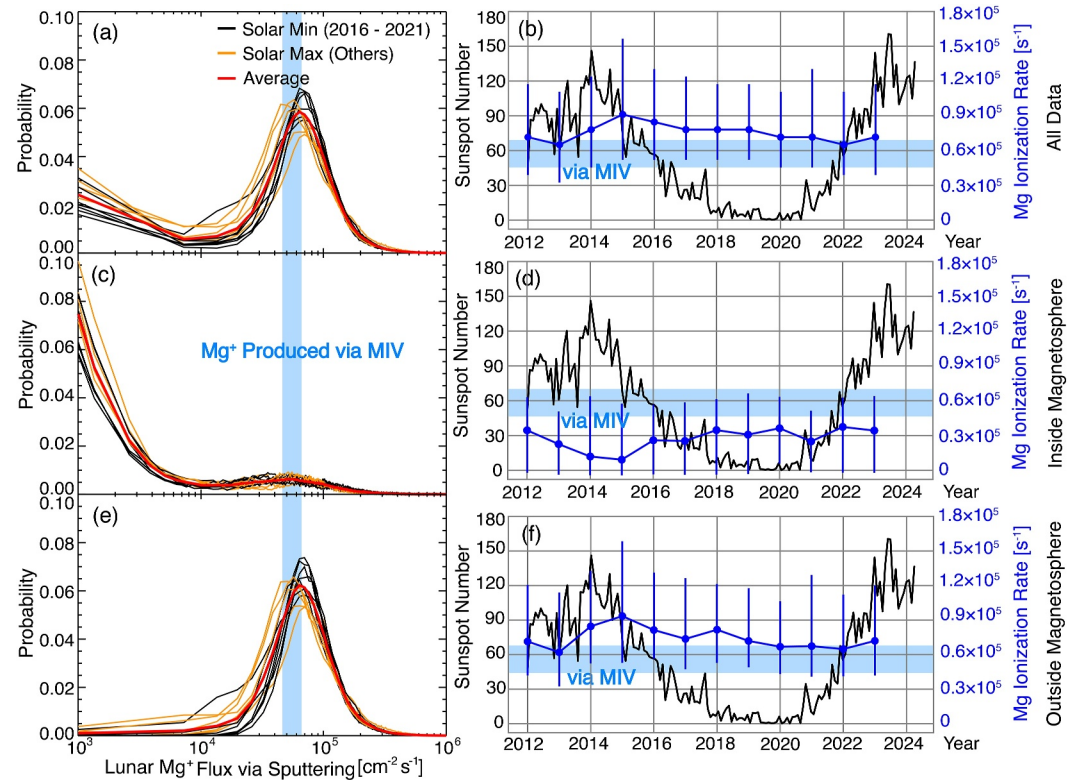
Figure 8. Distribution functions (a, c, and e), median, first and third quartiles (b, d, and f) of lunar Mg$^+$ fluxes via sputtering from the year 2012–2023. Lunar Mg$^+$ fluxes are categorized by the Moon's location in its orbit, including all data (top row), inside magnetosphere (middle row), and outside magnetosphere (bottom row). Distribution functions of Mg$^+$ fluxes (a, c, and e) are marked with black and orange in Solar Minimum (the year 2016–2021) and Solar Maximum (other years), respectively, and red for average distribution function for the 12 years. Box plots (b, d, and f) show the variations of sputtered Mg$^+$ fluxes versus solar activity, which is represented by the sunspot numbers. Data points are the median values of Mg$^+$ fluxes, and blue solid lines represent the IQRs. The blue boxes represent the Mg$^+$ fluxes produced via micrometeoroid impact vaporization.

4.2. Pickup Ion Fluxes

Figure 8 displays the distribution functions (a, c, e) and the median values along with the first and third quartiles (b, d, f) of lunar Mg$^+$ fluxes generated through sputtering for each year from 2012 to 2023. Consistent with Section 4.1, the data is categorized based on different locations of the Moon in its orbit, specifically when it is inside (c, d) and outside (e, f) the magnetosphere. The distribution functions (a, c, e) presented in Figure 8 exhibit similar characteristics to those in Figure 6, showing that the Mg$^+$ flux distribution functions resemble Maxwellian distribution functions with prolonged and increasing probability at lower flux values. These distribution functions consist of two parts, similar to the ionization rates: One part represents the decay function where Mg$^+$ fluxes are below 10^4 cm^{-2} s^{-1}, primarily occurring when the Moon is inside the magnetosphere. The other part follows a Maxwellian distribution, where Mg$^+$ fluxes exceed 10^4 cm^{-2} s^{-1}, mainly occurring when the Moon is outside the magnetosphere.

When comparing Mg$^+$ flux produced via MIV, represented by blue boxes in Figure 8, lunar Mg$^+$ fluxes are significantly higher by 50%–100% when the Moon is outside the magnetosphere, whereas they are lower by a factor of 2–3 when it is inside the magnetosphere. This comparison is consistent across the 12-year period and does not show a clear dependence on solar activity. The IQRs of Mg$^+$ fluxes, indicated by blue vertical solid lines, are influenced by solar activity and larger during solar maximum compared to solar minimum, indicating that Mg$^+$ flux distributions are more dispersed during solar maxima.
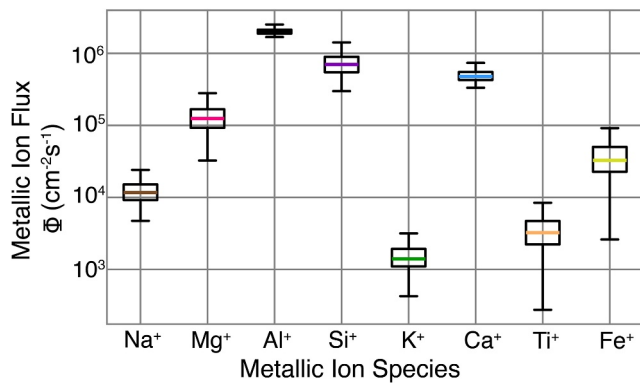
Figure 9. Box plots of lunar pickup ion flux for all the metallic ion species, including Na$^+$ (brown), Mg$^+$ (magenta), Al$^+$ (black), Si$^+$ (purple), K$^+$ (green), Ca$^+$ (blue), Ti$^+$ (orange) and Fe$^+$ (light green). Box plots indicate the minimum, first, second (median), third quartiles, and maximum values for lunar metallic ion fluxes.

4.3. Comparison Among Metallic Species

This study investigates not only the fluxes of lunar Mg$^+$ but also various metallic ion species that could potentially be produced from the lunar surface, including Na$^+$, Al$^+$, Si$^+$, K$^+$, Ca$^+$, Ti$^+$, and Fe$^+$. Figure 9 shows box plots of metallic ion fluxes, which indicate the minimum, first quartile, median, third quartile, and maximum values of metallic fluxes, with the length of the boxes representing the IQR. The primary metallic ions produced from the lunar surface are Al$^+$, Si$^+$, Ca$^+$, and Mg$^+$, with their fluxes typically ranging from 10^5 to 2×10^6 cm^{-2} s^{-1}. In contrast, the fluxes of other metallic species, including Na$^+$, K$^+$, Ti$^+$, and Fe$^+$, range from 10^3 to 10^5 cm^{-2} s^{-1}. Note that PSD generation is not included in this study; hence, Na$^+$ and K$^+$ fluxes are regarded as the lower limit. The variations in metallic ion fluxes suggest that the Moon's position significantly influences the abundance of lunar pickup ions, although their impacts differ by species. The maximum flux values are likely caused by geomagnetic storm activities that directly impact the lunar surface, whereas the minimum values generally occur when the Moon traverses the magnetotail. Al$^+$ fluxes show minimal variation, as evidenced by the IQR being close to the median value. The fluxes of most metallic ions vary by a factor of 2–5; however, Ti$^+$ and Fe$^+$ fluxes vary by more than an order of magnitude. These findings indicate that Al$^+$ is a more consistent source of metallic ions from the Moon, while Ti$^+$ and Fe$^+$ fluxes are more sensitive to the environment in which the Moon resides.

The metallic ion fluxes observed in this study are comparable in magnitude to those reported in previous modeling and observational studies. The total PUI fluxes are generally at the order of 10^6 cm^{-2} s^{-1}, as indicated by lunar PUI models (Poppe et al., 2022; Sarantos, Hartle, et al., 2012) and ARTEMIS data (Harada et al., 2015). Na$^+$ and K$^+$ fluxes in this study are estimated to be on the order of 10^3–10^4 cm^{-2} s^{-1}, agreeing with the Kaguya Magnetic field and Plasma experiment (MAP)-Plasma energy Angle and Composition experiment (PACE) measurement (Yokota et al., 2014). Furthermore, Al$^+$ and Si$^+$ are the predominant lunar pickup ion species, followed by mass-40 species (K$^+$, Ca$^+$ and ^{40}Ar$^+$), similar to the finding based on the LADEE NMS (Halekas et al., 2015).

5. Magnetospheric Metallic Ions: From Ionosphere or Moon?

The study of metallic ions from the Moon not only enhances our understanding of space weathering on the lunar surface but also significantly contributes to our knowledge of heavy ion species in the terrestrial environment. In the 1970s, the discovery of heavy ions (with atomic masses around 16 amu) in the magnetosphere indicated that the ionosphere could serve as a reservoir for magnetospheric plasma, which was previously thought to originate solely from the solar wind (Shelley et al., 1972). Since then, numerous studies have examined the contributions and circulation of ionospheric heavy ions in the magnetosphere, fostering a general belief that low-charge state heavy ions in the magnetosphere primarily come from the ionosphere (Dandouras, 2021; Kronberg et al., 2014; Toledo-Redondo et al., 2021). However, this may only apply to certain heavy ion species, especially those with masses greater than 16 amu. These species are typically categorized as metallic or molecular ions. Molecular ions are the predominant species in the ionosphere's E and F layers and thus, mainly sourced from the ionosphere. The presence of molecular ions in the magnetosphere is typically observed only in the high-altitude ionosphere and magnetosphere during periods of increased geomagnetic activity, suggesting that the mechanisms enabling their acceleration from eV to keV energies are closely linked to geomagnetic conditions (Klecker et al., 1986; Lin & Ilie, 2022; Seki et al., 2019).

Metallic ions, conversely, hold unique positions to provide insights into the circulation pathways of ionospheric outflow and the Earth-Moon interaction due to their low fluxes along both the source and transport routes in the magnetosphere (Christon et al., 2020; Yamauchi et al., 2024). Metallic ions can originate from two primary sources: (a) Earth's ionosphere, including those deposited by the ablation of meteoroids (Plane, 2012), and (b) the lunar exosphere, as discussed in this study. The relative contributions of these two sources to the magnetospheric metallic ion population remain uncertain, likely due to the limited capabilities of ion mass spectrometers on past and current spacecraft missions, which have restricted energy ranges (less than 50 eV and/or above 100 keV) and mass ranges (up to 40 amu). Fortunately, the outflow rate of metallic ions from Earth's ionosphere can be
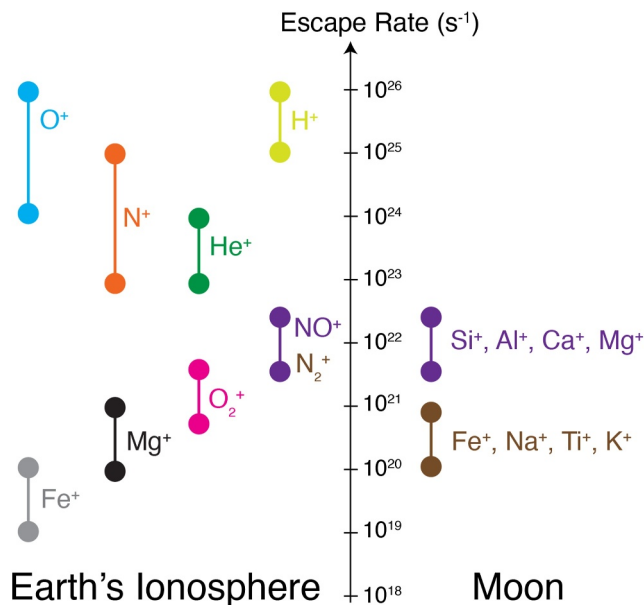
Figure 10. Ion escape rates from Earth's ionosphere (left panel) based on observational and modeling studies and Moon (right panel) from this study.

estimated through studies of molecular ions, as metallic and molecular ions have closely related masses. This study also offers potential input source rates for lunar-origin metallic ions, facilitating possible comparisons between the ionosphere and the lunar exosphere.

The ion escape rates from the ionosphere and Moon are derived to compare their relative contributions. Escape rates for ions originating from Earth's ionosphere, such as O^+ and H^+, have been extensively studied through previous observations using measurements from the Akebono (Cully et al., 2003), the Fast Auroral SnapshoT Explorer (FAST) (Andersson et al., 2005), Polar (Peterson et al., 2001), and Cluster (Schillings et al., 2019) missions with escape rates are approximated in the order of 10^{24}–10^{26} s^{-1}. The escape rates for He^+ and N^+ ions are based on modeling studies by Lin et al. (2020), where the N^+ density is approximately 10% of the O^+ density, and the densities of He^+ and N^+ are comparable. The escape rates for molecular ions, including N_2^+, NO^+, and O_2^+, are scaled from existing observational studies. Typically, molecular ion densities and fluxes range from about 0.1% to 10% of O^+ ions in the high-latitude ionosphere, as reported by ISIS-2 (J. H. Hoffman et al., 1974) and Akebono data (Peterson et al., 1994; Yau et al., 1993). Moreover, molecular N_2^+ and NO^+ ions are the dominant species among molecular ions, with their abundances exceeding those of O_2^+ by an order of magnitude (Lin et al., 2025). Since molecular ion outflow primarily occurs in the polar auroral and cusp regions, their escape rates are generally two to three orders of magnitude lower than those of O^+ (Lin & Ilie, 2022).

Ionosphere-origin metallic ions here are only considered as Mg^+ and Fe^+. Mg^+ ions (24 amu) represent metallic ions with masses between 20 and 30 amu (including Na^+, Mg^+, Al^+, and Si^+), while Fe^+ ions (56 amu) correspond to ions with masses between 40 and 60 amu (including Ca^+, K^+, Ti^+, and Fe^+). The escape rates for these ions are also scaled based on molecular ion escape rates, utilizing observed density ratios from existing studies. The ratio of $n(Fe^+)/n(Mg^+)$ has varied between 0.02 and 32, with metallic ions representing up to 10% of the molecular ion densities according to limited ground-based and spacecraft observations (J. Grebowsky et al., 1998; J. M. Grebowsky & Aikin, 2002; Kumar & Hanson, 1980; Granier et al., 1989). Thus, the escape rates for Mg^+ and Fe^+ from the terrestrial ionosphere are estimated to be one to two orders of magnitude lower than those for molecular ions.

Finally, the escape rates of lunar pickup ions (PUIs) are more straightforward to calculate, as they are based on derived fluxes illustrated in Figure 9. The escape rates for PUIs generated through neutral sputtering from the entire lunar surface are calculated by multiplying the sputtering fluxes with the incident sputtering area from which sputtering occurs. This calculation is influenced by the angles between the local lunar surface normal and the directions of solar wind impact. On the other hand, the escape rates for PUIs generated by MIV are simply determined by multiplying the fluxes by the lunar surface area.

Figure 10 summarizes and compares the ion escape rates from Earth's ionosphere and the Moon for various species. Ionospheric outflow is the primary source of heavy ions (M ≤ 16 amu) in the magnetosphere. As mentioned previously, the escape rates for H^+ and O^+ ions range from 10^{24} to 10^{26} s^{-1} (Andersson et al., 2005; Cully et al., 2003; Peterson et al., 2001; Schillings et al., 2019). Accordingly, the escape rates for N^+ and He^+ are approximated between 10^{23} and 10^{25} s^{-1}. The escape rates from the ionospheric outflow and lunar pickup ions become comparable for heavier ions with masses greater than 16. The escape rates of metallic ions from the Moon are similar to those of molecular ions escaping from Earth's ionosphere, both at approximately 10^{22} s^{-1}. Notably, the escape rates of metallic ions such as Mg^+ and Fe^+ from the Moon are an order of magnitude higher than those from Earth's ionosphere. These comparisons indicate that lunar pickup ions may play a significant role as a source of heavy ions in the terrestrial environment. The ambiguity between metallic and molecular ions in the magnetosphere could aid in interpreting measurements of heavy ions. A statistical analysis using data from the Arase satellite over 6 years reveals that heavy ions with masses around 28 amu show that long-term variations in molecular ions differ from those of the O^+ and N^+ groups (Nagatani et al., 2024). While this difference may be

attributed to variations in ionospheric chemistry, it could also be due to the mixing of heavy ions with masses around 28 amu with lunar-origin metallic ions and ionospheric molecular ions.

6. Conclusion

This study analyzes the abundance of lunar metallic ions and their variations in response to the Moon's position in its orbit, using the PUI model of Poppe et al. (2022), along with information about the cis-lunar environment derived from THEMIS-ARTEMIS observational data. The main findings are summarized below:

- When the Moon is in solar wind upstream regions, lunar metallic ions primarily originate from the ionization of neutrals sputtered from the lunar surface. On the other hand, when the Moon crosses into the magnetosphere, lunar metallic ions are predominantly sourced from the ionization of neutrals produced through MIV rather than by sputtering.
- The average production rate of lunar metallic ions remains generally constant regardless of the solar cycle. Overall, Al^+ and Si^+ are the predominant metallic pickup ion species, with fluxes $\sim 10^6$ cm^{-2} s^{-1}.
- The total escape rate of metallic ions from the Moon is $\sim 10^{23}$ s^{-1}, comparable to the total escape rate of molecular and metallic ions from Earth's ionosphere. Furthermore, metallic ion escape rates originating from the Moon are larger by an order of magnitude than those from the ionosphere.

Past observations of singly-charge heavy ions (with mass ~ 28 amu) in Earth's magnetosphere were assumed to consist of molecular N_2^+ and NO^+ ions sourced from the ionosphere (Lin & Ilie, 2022), and metallic ions, such as Si^+ and Fe^+, from the ablation of meteoroids (Christon et al., 2017). However, the comparable rates of both molecular and metallic ions from Earth's ionosphere and the Moon, as suggested by this study, indicate a need to re-evaluate the observations of heavy ions, especially those with masses ~ 28 amu, in order to understand their origins and transport pathways. Figure 10 shows that the fluxes of lunar Mg^+ and Fe^+ are typically an order of magnitude higher than the outflowing fluxes of Mg^+ and Fe^+ from Earth's ionosphere. These findings suggest that the metallic ions observed by the Geotail spacecraft may originate from the Moon's pickup ions and Earth's ionospheric outflow. Furthermore, the similar contributions from Earth's ionosphere and the lunar exosphere complicate the identification of magnetospheric heavy ions with masses close to 28 amu, as detected by Geotail (Christon et al., 2020) and Arase (Nagatani et al., 2024). These ions may be either ionospheric molecular N_2^+ and NO^+ ions or lunar metallic Al^+ and Si^+ ions, given their significant roles in the ionosphere and lunar exosphere. Performing dynamical tracing of the trajectories of lunar-originating metallic pickup ions throughout the magnetosphere is critical to assessing whether or not lunar metallic ions can propagate throughout the magnetosphere and potentially contribute to existing observations of metallic ions (e.g., Christon et al., 2017, 2020).

This study investigates the temporal evolution of lunar pickup ion fluxes along the lunar orbit and, for the first time, compares the contributions from the ionosphere and lunar exosphere with previous terrestrial spacecraft missions. Tracking pickup ions and their temporal variations enhances our understanding of lunar space weathering. Furthermore, investigating the lunar pickup ions during interplanetary shocks, as well as the passage of CMEs and corotating interaction regions (CIRs), has gained importance in the context of current and upcoming human exploration missions, including ARTEMIS and HERMES. Additionally, the contributions of lunar plasma to the terrestrial environment have potentially been underestimated in studies of Earth's magnetosphere. The comparable production rates of the ionosphere and lunar plasma, especially for heavy ions with masses over 16 amu, as highlighted in this study, underscores the necessity to reassess magnetospheric heavy ions, which has been recently made by Yamauchi et al. (2024). This also emphasizes the need for advanced instrument technology and new missions to gain insights into the circulation of heavy ions in the Earth-Moon system.

Data Availability Statement

All the data used in this paper is publicly available. ARTEMIS data are available at Coordinated Data Analysis Web (CDAWeb) in NASA's Space Physics Data Facility (SPDF) platform of GSFC at https://cdaweb.gsfc.nasa.gov/pub/data/themis/. The data and scripts used in the production of all figures have been made available online in Lin and Poppe (2025).

References

Andersson, L., Peterson, W. K., & McBryde, K. M. (2005). Estimates of the suprathermal o+ outflow characteristic energy and relative location in the auroral oval. *Geophysical Research Letters*, *32*(9). https://doi.org/10.1029/2004GL021434

Angelopoulos, V. (2010). The Artemis mission. *Space Science Reviews*, *165*(1–4), 1–23. https://doi.org/10.1007/s11214-010-9687-2

Auster, H., Glassmeier, K., Magnes, W., Aydogar, O., Baumjohann, W., Constantinescu, D., et al. (2008). The THEMIS fluxgate magnetometer. *Space Science Reviews*, *141*, 235–264. https://doi.org/10.1007/978-0-387-89820-9_11

Barghouty, A., Meyer, F., Harris, P., & Adams, J. (2011). Solar-wind protons and heavy ions sputtering of lunar surface materials. *Nuclear Instruments and Methods in Physics Research Section B: Beam Interactions with Materials and Atoms*, *269*(11), 1310–1315. https://doi.org/10.1016/j.nimb.2010.12.033

Bartlett, P. L., & Stelbovics, A. T. (2002). Calculation of electron-impact total-ionization cross sections. *Physical Review A*, *66*(1), 012707. https://doi.org/10.1103/physreva.66.012707

Bartlett, P. L., & Stelbovics, A. T. (2004). Electron-impact ionization cross sections for elements Z=1 to Z=54. *Atomic Data and Nuclear Data Tables*, *86*(2), 235–265. https://doi.org/10.1016/j.adt.2003.11.006

Baumgardner, J., Luettgen, S., Schmidt, C., Mayyasi, M., Smith, S., Martinis, C., et al. (2021). Long-term observations and physical processes in the moon's extended sodium tail. *Journal of Geophysical Research: Planets*, *126*(3), e2020JE006671. https://doi.org/10.1029/2020JE006671

Benna, M., Mahaffy, P. R., Halekas, J. S., Elphic, R. C., & Delory, G. T. (2015). Variability of helium, neon, and argon in the lunar exosphere as observed by the LADEE NMS instrument. *Geophysical Research Letters*, *42*(10), 3723–3729. https://doi.org/10.1002/2015GL064120

Biersack, J., & Eckstein, W. (1984). Sputtering studies with the Monte Carlo program trim. Sp. *Applied Physics A*, *34*(2), 73–94. https://doi.org/10.1007/bf00614759

Bonnell, J., Mozer, F., Delory, G., Hull, A., Ergun, R., Cully, C., et al. (2009). The Electric Field Instrument (EFI) for THEMIS. *Space Science Reviews*, 303–341. https://doi.org/10.1007/978-0-387-89820-9_14

Cao, X., Halekas, J. S., Chu, F., Kistler, M., Poppe, A. R., & Glassmeier, K.-H. (2020). Plasma convection in the terrestrial magnetotail lobes measured near the moon's orbit. *Geophysical Research Letters*, *47*(20), e2020GL090217. https://doi.org/10.1029/2020GL090217

Christon, S. P., Hamilton, D. C., Mitchell, D. G., Plane, J. M. C., & Nylund, S. R. (2020). Suprathermal magnetospheric atomic and molecular heavy ions at and near Earth, Jupiter, and Saturn: Observations and identification. *Journal of Geophysical Research: Space Physics*, *125*(1), e27271. https://doi.org/10.1029/2019ja027271

Christon, S. P., Hamilton, D. C., Plane, J. M. C., Mitchell, D. G., Grebowsky, J. M., Spjeldvik, W. N., & Nylund, S. R. (2017). Discovery of suprathermal ionospheric origin Fe+ in and near earth's magnetosphere. *Journal of Geophysical Research: Space Physics*, *122*(11), 175–200. https://doi.org/10.1002/2017JA024414

Collette, A., Drake, K., Mocker, A., Sternovsky, Z., Munsat, T., & Horanyi, M. (2013). Time-resolved temperature measurements in hyper-velocity dust impact. *Planetary and Space Science*, *89*, 58–62. https://doi.org/10.1016/j.pss.2013.02.007

Cully, C. M., Donovan, E., Yau, A. W., & Arkos, G. G. (2003). Akebono/Suprathermal Mass Spectrometer observations of low-energy ion outflow: Dependence on magnetic activity and solar wind conditions. *Journal of Geophysical Research*, *108*(A2), 1093. https://doi.org/10.1029/2001JA009200

Dandouras, I. (2021). Ion outflow and escape in the terrestrial magnetosphere: Cluster advances. *Journal of Geophysical Research: Space Physics*, *126*(10), e2021JA029753. https://doi.org/10.1029/2021JA029753

Denevi, B. W., Noble, S. K., Christoffersen, R., Thompson, M. S., Glotch, T. D., Blewett, D. T., et al. (2023). Space weathering at the Moon. *Reviews in Mineralogy and Geochemistry*, *89*(1), 611–650. https://doi.org/10.2138/rmg.2023.89.14

Ebel, F., & Salzborn, E. (1987). Charge transfer of 0.2-5.0 keV protons and hydrogen atoms in sodium-potassium-and Rubidium-Vapour targets. *Journal of Physics B: Atomic and Molecular Physics*, *20*(17), 4531–4542. https://doi.org/10.1088/0022-3700/20/17/029

Eichhorn, G. (1976). Analysis of the hypervelocity impact process from impact flash measurements. *Planetary and Space Science*, *24*(8), 771–781. https://doi.org/10.1016/0032-0633(76)90114-8

Eichhorn, G. (1978). Heating and vaporization during hypervelocity particle impact. *Planetary and Space Science*, *26*(5), 463–467. https://doi.org/10.1016/0032-0633(78)90067-3

Elphic, R. C., Funsten III, H. O., Barraclough, B. L., McComas, D. J., Paffett, M. T., Vaniman, D. T., & Heiken, G. (1991). Lunar surface composition and solar wind-induced secondary ion mass spectrometry. *Geophysical Research Letters*, *18*(11), 2165–2168. https://doi.org/10.1029/91GL02669

Gamborino, D., & Wurz, P. (2018). Velocity distribution function of Na released by photons from planetary surfaces. *Planetary and Space Science*, *159*, 97–104. https://doi.org/10.1016/j.pss.2018.04.021

Gopalswamy, N., Yashiro, S., Akiyama, S., Xie, H., Mäkelä, P., Fok, M.-C., & Ferradas, C. P. (2022). What is unusual about the third largest geomagnetic storm of Solar Cycle 24? *Journal of Geophysical Research: Space Physics*, *127*(8), e2022JA030404. https://doi.org/10.1029/2022ja030404

Granier, C., Jégou, J.-P., & Megie, G. (1989). Iron atoms and metallic species in the earth's upper atmosphere. *Geophysical Research Letters*, *16*(3), 243–246. https://doi.org/10.1029/gl016i003p00243

Grava, C., Hurley, D. M., Feldman, P. D., Retherford, K. D., Greathouse, T. K., Pryor, W. R., et al. (2020). LRO/LAMP observations of the lunar helium exosphere: Constraints on thermal accommodation and outgassing rate. *Monthly Notices of the Royal Astronomical Society*, *501*(3), 4438–4451. https://doi.org/10.1093/mnras/staa3884

Grebowsky, J., Goldberg, R., & Pesnell, W. (1998). Do meteor showers significantly perturb the ionosphere? *Journal of Atmospheric and Solar-Terrestrial Physics*, *60*(6), 607–615. https://doi.org/10.1016/s1364-6826(98)00004-2

Grebowsky, J. M., & Aikin, A. C. (2002). In situ measurements of meteoric ions. *Meteors in the Earth's Atmosphere*, 189–214.

Haaland, S., Daly, P. W., & Vilenius, E. (2021). Heavy metal and rock in space: Cluster rapid observations of fe and si. *Journal of Geophysical Research: Space Physics*, *126*(3). https://doi.org/10.1029/2020ja028852

Halekas, J. S., Benna, M., Mahaffy, P. R., Elphic, R. C., Poppe, A. R., & Delory, G. T. (2015). Detections of lunar exospheric ions by the LADEE neutral mass spectrometer. *Geophysical Research Letters*, *42*(13), 5162–5169. https://doi.org/10.1002/2015GL064746

Halekas, J. S., Delory, G. T., Farrell, W. M., Angelopoulos, V., McFadden, J. P., Bonnell, J. W., et al. (2011). First remote measurements of lunar surface charging from ARTEMIS: Evidence for nonmonotonic sheath potentials above the dayside surface. *Journal of Geophysical Research*, *116*(A7). https://doi.org/10.1029/2011JA016542

Halekas, J. S., Poppe, A. R., Delory, G. T., Sarantos, M., Farrell, W. M., Angelopoulos, V., & McFadden, J. P. (2012). Lunar pickup ions observed by ARTEMIS: Spatial and temporal distribution and constraints on species and source locations. *Journal of Geophysical Research*, *117*(E6). https://doi.org/10.1029/2012JE004107

Halekas, J. S., Poppe, A. R., Farrell, W. M., & McFadden, J. P. (2016). Structure and composition of the distant lunar exosphere: Constraints from ARTEMIS observations of ion acceleration in time-varying fields. *Journal of Geophysical Research: Planets*, *121*(6), 1102–1115. https://doi.org/10.1002/2016JE005082

Halekas, J. S., Poppe, A. R., Harada, Y., Bonnell, J. W., Ergun, R. E., & McFadden, J. P. (2018). A tenuous lunar ionosphere in the geomagnetic tail. *Geophysical Research Letters*, *45*(18), 9450–9459. https://doi.org/10.1029/2018GL079936

Halekas, J. S., Poppe, A. R., & McFadden, J. P. (2014). The effects of solar wind velocity distributions on the refilling of the lunar wake: ARTEMIS observations and comparisons to one-dimensional theory. *Journal of Geophysical Research: Space Physics*, *119*(7), 5133–5149. https://doi.org/10.1002/2014JA020083

Hapke, B. (2001). Space weathering from Mercury to the asteroid belt. *Journal of Geophysical Research*, *106*(E5), 10039–10073. https://doi.org/10.1029/2000JE001338

Hapke, B., Cohen, A., Cassidy, W., & Wells, E. (1970). Solar radiation effects in lunar samples. *Science*, *167*(3918), 745–747. https://doi.org/10.1126/science.167.3918.745

Harada, Y., Halekas, J. S., Poppe, A. R., Tsugawa, Y., Kurita, S., & McFadden, J. P. (2015). Statistical characterization of the foremoon particle and wave morphology: ARTEMIS observations. *Journal of Geophysical Research: Space Physics*, *120*(6), 4907–4921. https://doi.org/10.1002/2015JA021211

Hartle, R. E., & Killen, R. (2006). Measuring pickup ions to characterize the surfaces and exospheres of planetary bodies: Applications to the Moon. *Geophysical Research Letters*, *33*(5). https://doi.org/10.1029/2005GL024520

Heiken, G., Vaniman, D., & French, B. M. (1991). *Lunar sourcebook: A user's guide to the Moon* (Vol. No. 1259). Cup Archive.

Hendrix, A. R., Hurley, D. M., Farrell, W. M., Greenhagen, B. T., Hayne, P. O., Retherford, K. D., et al. (2019). Diurnally Migrating lunar water: Evidence from Ultraviolet data. *Geophysical Research Letters*, *46*(5), 2417–2424. https://doi.org/10.1029/2018GL081821

Hilchenbach, M., Hovestadt, D., Klecker, B., & Möbius, E. (1992). Detection of singly ionized energetic lunar pick-up ions upstream of Earth's bow shock. In E. Marsch & R. Schwenn (Eds.), *Solar wind seven* (pp. 349–355). Pergamon. https://doi.org/10.1016/B978-0-08-042049-3.50075-2

Hilchenbach, M., Hovestadt, D., Klecker, B., & Möbius, E. (1993). Observation of energetic lunar pick-up ions near Earth. *Advances in Space Research*, *13*(10), 321–324. https://doi.org/10.1016/0273-1177(93)90086-Q

Hodges, R., Hoffman, J., & Johnson, F. S. (1974). The lunar atmosphere. *Icarus*, *21*(4), 415–426. https://doi.org/10.1016/0019-1035(74)90144-4

Hodges Jr, R. R. (1980). Lunar cold traps and their influence on argon-40. In *Lunar and planetary science conference, 11th, Houston, TX, March 17-21, 1980, proceedings. Volume 3.(a82-22351 09-91)* (Vol. 11, pp. 2463–2477). Pergamon Press.

Hoffman, J., Hodges, R., Johnson, F., & Evans, D. (1973). Lunar atmospheric composition results from Apollo 17. *Lunar planet Science Conference* (Vol. 4, 376).

Hoffman, J. H., Dodson, W. H., Lippincott, C. R., & Hammack, H. D. (1974). Initial ion composition results from the Isis 2 satellite. *Journal of Geophysical Research*, *79*(28), 4246–4251. https://doi.org/10.1029/ja079i028p04246

Holmström, M., Fatemi, S., Futaana, Y., & Nilsson, H. (2012). The interaction between the Moon and the solar wind. *Earth Planets and Space*, *64*(2), 237–245. https://doi.org/10.5047/eps.2011.06.040

Huebner, W., & Mukherjee, J. (2015). Photoionization and photodissociation rates in solar and blackbody radiation fields. *Planetary and Space Science*, *106*, 11–45. https://doi.org/10.1016/j.pss.2014.11.022

Huebner, W. F., & Carpenter, C. (1979). *Solar photo rate coefficients*. Los Alamos Scientific Laboratory.

Huebner, W. F., Keady, J. J., & Lyon, S. (1992). *Solar photo rates for planetary atmospheres and atmospheric pollutants*. Springer.

Hunten, D., Cremonese, G., Sprague, A., Hill, R., Verani, S., & Kozlowski, R. (1998). The leonid meteor shower and the lunar sodium atmosphere. *Icarus*, *136*(2), 298–303. https://doi.org/10.1006/icar.1998.6023

Hunten, D., & Sprague, A. (1997). Origin and character of the lunar and mercurian atmospheres. *Advances in Space Research*, *19*(10), 1551–1560. https://doi.org/10.1016/S0273-1177(97)00368-2

Hurley, D. M., Cook, J. C., Retherford, K. D., Greathouse, T., Gladstone, G. R., Mandt, K., et al. (2017). Contributions of solar wind and micrometeoroids to molecular hydrogen in the lunar exosphere. *Icarus*, *283*, 31–37. https://doi.org/10.1016/j.icarus.2016.04.019

Janches, D., Berezhnoy, A. A., Christou, A. A., Cremonese, G., Hirai, T., Horányi, M., et al. (2021). Meteoroids as one of the sources for exosphere formation on airless bodies in the inner solar system. *Space Science Reviews*, *217*(4), 1–41. https://doi.org/10.1007/s11214-021-00827-6

Jr Hodges, R., Hoffman, J., Johnson, F., & Evans, D. (1973). Composition and dynamics of lunar atmosphere. *Proceedings of the lunar science conference* (Vol. 4, 2855).

Kagitani, M., Taguchi, M., Yamazaki, A., Yoshikawa, I., Murakami, G., Yoshioka, K., et al. (2010). Variation in lunar sodium exosphere measured from lunar orbiter SELENE (Kaguya). *Planetary and Space Science*, *58*(12), 1660–1664. https://doi.org/10.1016/j.pss.2010.07.025

Kallio, E., & Facskó, G. (2015). Properties of plasma near the moon in the magnetotail. *Planetary and Space Science*, *115*, 69–76. https://doi.org/10.1016/j.pss.2014.11.007

Kasper, J. C., Stevens, M. L., Lazarus, A. J., Steinberg, J. T., & Ogilvie, K. W. (2007). Solar wind helium abundance as a function of speed and heliographic latitude: Variation through a solar cycle. *The Astrophysical Journal*, *660*(1), 901–910. https://doi.org/10.1086/510842

Killen, R. M. (2002). Source and maintenance of the argon atmospheres of Mercury and the Moon. *Meteoritics & Planetary Science*, *37*(9), 1223–1231. https://doi.org/10.1111/j.1945-5100.2002.tb00891.x

Killen, R. M., Hurley, D. M., & Farrell, W. M. (2012). The effect on the lunar exosphere of a coronal mass ejection passage. *Journal of Geophysical Research*, *117*(E10). https://doi.org/10.1029/2011JE004011

Killen, R. M., & Ip, W.-H. (1999). The surface-bounded atmospheres of Mercury and the Moon. *Reviews of Geophysics*, *37*(3), 361–406. https://doi.org/10.1029/1999RG900001

Kirsch, E., Wilken, B., Gloeckler, G., Galvin, A., Mall, U., & Hovestadt, D. (1997). Comparison of lunar and terrestrial ion measurements obtained by the Wind and GEOTAIL spacecraft outside and inside the Earth's magnetosphere. *Advances in Space Research*, *20*(4), 845–849. https://doi.org/10.1016/S0273-1177(97)00518-8

Klecker, B., Möbius, E., Hovestadt, D., Scholer, M., Gloeckler, G., & Ipavich, F. M. (1986). Discovery of energetic molecular ions (no+ and o2+) in the storm time ring current. *Geophysical Research Letters*, *13*(7), 632–635. https://doi.org/10.1029/GL013i007p00632

Kronberg, E. A., Ashour-Abdalla, M., Dandouras, I., Delcourt, D. C., Grigorenko, E. E., Kistler, L. M., et al. (2014). Circulation of heavy ions and their dynamical effects in the magnetosphere: Recent observations and models. *Space Science Reviews*, *184*(1–4), 173–235. https://doi.org/10.1007/s11214-014-0104-0

Kumar, S., & Hanson, W. (1980). The morphology of metallic ions in the upper atmosphere. *Journal of Geophysical Research*, *85*(A12), 6783–6801. https://doi.org/10.1029/ja085ia12p06783

Li, S., Poppe, A., Orlando, T., Jones, B., Tucker, O., Farrell, W., & Hendrix, A. (2023). Formation of lunar surface water associated with high-energy electrons in earth's magnetotail. *Nature Astronomy*, *7*(12), 1427–1435. https://doi.org/10.1038/s41550-023-02081-y

Lin, M.-Y., & Ilie, R. (2022). A review of observations of molecular ions in the earth's magnetosphere-ionosphere system. *Frontiers in Astronomy and Space Sciences*, *8*. https://doi.org/10.3389/fspas.2021.745357

Lin, M.-Y., Ilie, R., & Glocer, A. (2020). The contribution of n+ ions to earth's polar wind. *Geophysical Research Letters*, *47*(18), e2020GL089321. https://doi.org/10.1029/2020GL089321

Lin, M.-Y., Ilie, R., & Glocer, A. (2025). Limits on the efficacy of wave-particle interaction on the energization and transport of atomic and molecular heavy ionospheric ions. *Journal of Geophysical Research: Space Physics*, *130*(4), e2024JA033523. https://doi.org/10.1029/2024ja033523

Lin, M.-Y., & Poppe, A. R. (2025). Metallic ions near the moon: Impact of solar activity and lunar position [Dataset]. *Zenodo*. https://doi.org/10.5281/zenodo.14873527

Liuzzo, L., Poppe, A. R., & Halekas, J. S. (2022). A statistical study of the moon's magnetotail plasma environment. *Journal of Geophysical Research: Space Physics*, *127*(4), e2022JA030260. https://doi.org/10.1029/2022JA030260

Mahaffy, P. R., Richard Hodges, R., Benna, M., King, T., Arvey, R., & Barciniak, M. (2015). *The neutral mass spectrometer on the lunar atmosphere and Dust environment explorer mission* (pp. 27–61). The Lunar Atmosphere and Dust Environment Explorer Mission (LADEE).

Mall, U., Kirsch, E., Cierpka, K., Wilken, B., Söding, A., Neubauer, F., et al. (1998). Direct observation of lunar pick-up ions near the moon. *Geophysical Research Letters*, *25*(20), 3799–3802. https://doi.org/10.1029/1998GL900003

Manka, R., & Michel, F. (1973). Lunar ion flux and energy. In *Photon and particle interactions with surfaces in space: Proceedings of the 6th Eslab symposium, held at Noordwijk, the Netherlands, 26–29 September* (Vol. 1972, 429–442). https://doi.org/10.1007/978-94-010-2647-5_28

McComas, D., Angold, N., Elliott, H., Livadiotis, G., Schwadron, N., Skoug, R., & Smith, C. (2013). Weakest solar wind of the space age and the current "mini" solar maximum. *The Astrophysical Journal*, *779*(1), 2. https://doi.org/10.1088/0004-637x/779/1/2

McFadden, J., Carlson, C., Larson, D., Ludlam, M., Abiad, R., Elliott, B., et al. (2008). The THEMIS ESA plasma instrument and in-flight calibration. *Space Science Reviews*, *141*, 277–302. https://doi.org/10.1007/978-0-387-89820-9_13

Morgan, T., Olson, R. E., Schlachter, A., & Gallagher, J. (1985). Charge transfer of hydrogen ions and atoms in metal vapors. *Journal of Physical and Chemical Reference Data*, *14*(4), 971–1040. https://doi.org/10.1063/1.555752

Nagatani, A., Miyoshi, Y., Asamura, K., Kistler, L. M., Nakamura, S., Seki, K., et al. (2024). Variation of molecular ions in the inner magnetosphere observed by the arase satellite. *Geophysical Research Letters*, *51*(18), e2024GL108340. https://doi.org/10.1029/2024GL108340

Nie, N. X., Dauphas, N., Zhang, Z. J., Hopp, T., & Sarantos, M. (2024). Lunar soil record of atmosphere loss over eons. *Science Advances*, *10*(31), eadm7074. https://doi.org/10.1126/sciadv.adm7074

Papike, J. J., Simon, S. B., & Laul, J. C. (1982). The lunar regolith: Chemistry, mineralogy, and petrology. *Reviews of Geophysics*, *20*(4), 761–826. https://doi.org/10.1029/RG020i004p00761

Peterson, W. K., Abe, T., Fukunishi, H., Greffen, M. J., Hayakawa, H., Kasahara, Y., et al. (1994). On the sources of energization of molecular ions at ionospheric altitudes. *Journal of Geophysical Research*, *99*(A12), 23257–23274. https://doi.org/10.1029/94JA01738

Peterson, W. K., Collin, H. L., Yau, A. W., & Lennartsson, O. W. (2001). Polar/toroidal imaging mass-angle spectrograph observations of suprathermal ion outflow during solar minimum conditions. *Journal of Geophysical Research*, *106*(A4), 6059–6066. https://doi.org/10.1029/2000JA003006

Pieters, C. M., & Noble, S. K. (2016). Space weathering on airless bodies. *Journal of Geophysical Research: Planets*, *121*(10), 1865–1884. https://doi.org/10.1002/2016JE005128

Plane, J. M. (2012). Cosmic dust in the earth's atmosphere. *Chemical Society Reviews*, *41*(19), 6507–6518. https://doi.org/10.1039/c2cs35132c

Pokorný, P., Janches, D., Sarantos, M., Szalay, J. R., Horányi, M., Nesvorný, D., & Kuchner, M. J. (2019). Meteoroids at the moon: Orbital properties, surface vaporization, and impact ejecta production. *Journal of Geophysical Research: Planets*, *124*(3), 752–778. https://doi.org/10.1029/2018JE005912

Poppe, A. R., Farrell, W. M., & Halekas, J. S. (2018). Formation timescales of amorphous rims on lunar grains derived from Artemis observations. *Journal of Geophysical Research: Planets*, *123*(1), 37–46. https://doi.org/10.1002/2017JE005426

Poppe, A. R., Halekas, J. S., & Harada, Y. (2022). A comprehensive model for pickup ion formation at the moon. *Journal of Geophysical Research: Planets*, *127*(10), e2022JE007422. https://doi.org/10.1029/2022JE007422

Poppe, A. R., Halekas, J. S., Lue, C., & Fatemi, S. (2017). Artemis observations of the solar wind proton scattering function from lunar crustal magnetic anomalies. *Journal of Geophysical Research: Planets*, *122*(4), 771–783. https://doi.org/10.1002/2017JE005313

Poppe, A. R., Halekas, J. S., Samad, R., Sarantos, M., & Delory, G. T. (2013). Model-based constraints on the lunar exosphere derived from Artemis pickup ion observations in the terrestrial magnetotail. *Journal of Geophysical Research: Planets*, *118*(5), 1135–1147. https://doi.org/10.1002/jgre.20090

Poppe, A. R., Halekas, J. S., Sarantos, M., & Delory, G. T. (2013). The self-sputtered contribution to the lunar exosphere. *Journal of Geophysical Research: Planets*, *118*(9), 1934–1944. https://doi.org/10.1002/jgre.20148

Poppe, A. R., Halekas, J. S., Szalay, J. R., Horányi, M., Levin, Z., & Kempf, S. (2016). Ladee/ldex observations of lunar pickup ion distribution and variability. *Geophysical Research Letters*, *43*(7), 3069–3077. https://doi.org/10.1002/2016GL068393

Poppe, A. R., Samad, R., Halekas, J. S., Sarantos, M., Delory, G. T., Farrell, W. M., et al. (2012). Artemis observations of lunar pick-up ions in the terrestrial magnetotail lobes. *Geophysical Research Letters*, *39*(17). https://doi.org/10.1029/2012GL052909

Potter, A. E., & Morgan, T. H. (1998). Coronagraphic observations of the lunar sodium exosphere near the lunar surface. *Journal of Geophysical Research*, *103*(E4), 8581–8586. https://doi.org/10.1029/98JE00059

Rutherford, J., & Vroom, D. (1972). Formation of iron ions by charge transfer. *The Journal of Chemical Physics*, *57*(8), 3091–3093. https://doi.org/10.1063/1.1678724

Sarantos, M., Hartle, R. E., Killen, R. M., Saito, Y., Slavin, J. A., & Glocer, A. (2012). Flux estimates of ions from the lunar exosphere. *Geophysical Research Letters*, *39*(13). https://doi.org/10.1029/2012GL052001

Sarantos, M., Killen, R. M., Glenar, D. A., Benna, M., & Stubbs, T. J. (2012). Metallic species, oxygen and silicon in the lunar exosphere: Upper limits and prospects for Ladee measurements. *Journal of Geophysical Research*, *117*(A3). https://doi.org/10.1029/2011JA017044

Schillings, A., Slapak, R., Nilsson, H., Yamauchi, M., Dandouras, I., & Westerberg, L.-G. (2019). Earth atmospheric loss through the plasma mantle and its dependence on solar wind parameters. *Earth Planets and Space*, *71*(1), 1–13. https://doi.org/10.1186/s40623-019-1048-0

Schorghofer, N., Williams, J.-P., Martinez-Camacho, J., Paige, D. A., & Siegler, M. A. (2021). Carbon dioxide cold traps on the Moon. *Geophysical Research Letters*, *48*(20), e2021GL095533. https://doi.org/10.1029/2021GL095533

Schwenn, R. (2007). Solar wind sources and their variations over the solar cycle. *Solar dynamics and its effects on the heliosphere and Earth*, 51–76. https://doi.org/10.1007/978-0-387-69532-7_5

Seki, K., Keika, K., Kasahara, S., Yokota, S., Hori, T., Asamura, K., et al. (2019). Statistical properties of molecular ions in the ring current observed by the Arase (erg) satellite. *Geophysical Research Letters*, *46*(15), 8643–8651. https://doi.org/10.1029/2019gl084163

Shelley, E. G., Johnson, R. G., & Sharp, R. D. (1972). Satellite observations of energetic heavy ions during a geomagnetic storm. *Journal of Geophysical Research*, *77*(31), 6104–6110. https://doi.org/10.1029/JA077i031p06104

Shen, H.-W., Halekas, J. S., & Poppe, A. R. (2024). Dependence of lunar pickup Ion flux on source location: ARTEMIS observations. *The Astrophysical Journal*, *967*(2), 84. https://doi.org/10.3847/1538-4357/ad40a4

Sigmund, P. (1969). Theory of sputtering. I. Sputtering yield of amorphous and polycrystalline targets. *Physical review*, *184*(2), 383–416. https://doi.org/10.1103/physrev.184.383

Smyth, W. H., & Marconi, M. (1995). Theoretical overview and modeling of the sodium and potassium atmospheres of the moon. *Astrophysical Journal, Part 1*, *443*(1), 371–392. https://doi.org/10.1086/175532

Stern, S. A. (1999). The lunar atmosphere: History, status, current problems, and context. *Reviews of Geophysics*, *37*(4), 453–491. https://doi.org/10.1029/1999rg900005

Stern, S. A., Cook, J. C., Chaufray, J. Y., Feldman, P. D., Gladstone, G. R., & Retherford, K. D. (2013). Lunar atmospheric h2 detections by the lamp UV spectrograph on the lunar reconnaissance orbiter. *Icarus*, *226*(2), 1210–1213. https://doi.org/10.1016/j.icarus.2013.07.011

Szabo, P. S., Biber, H., Jäggi, N., Brenner, M., Weichselbaum, D., Niggas, A., et al. (2020). Dynamic potential sputtering of lunar analog material by solar wind ions. *The Astrophysical Journal*, *891*(1), 100. https://doi.org/10.3847/1538-4357/ab7008

Szalay, J. R., & Horányi, M. (2015). Annual variation and synodic modulation of the sporadic meteoroid flux to the Moon. *Geophysical Research Letters*, *42*(24), 580–584. https://doi.org/10.1002/2015GL066908

Szalay, J. R., Horányi, M., Colaprete, A., & Sarantos, M. (2016). Meteoritic influence on sodium and potassium abundance in the lunar exosphere measured by LADEE. *Geophysical Research Letters*, *43*(12), 6096–6102. https://doi.org/10.1002/2016GL069541

Tanaka, T., Saito, Y., Yokota, S., Asamura, K., Nishino, M. N., Tsunakawa, H., et al. (2009). First in situ observation of the Moon-originating ions in the Earth's Magnetosphere by MAP-PACE on SELENE (KAGUYA). *Geophysical Research Letters*, *36*(22). https://doi.org/10.1029/2009GL040682

Tenishev, V., Rubin, M., Tucker, O. J., Combi, M. R., & Sarantos, M. (2013). Kinetic modeling of sodium in the lunar exosphere. *Icarus*, *226*(2), 1538–1549. https://doi.org/10.1016/j.icarus.2013.08.021

Thompson, M. W. (1968). II. The energy spectrum of ejected atoms during the high energy sputtering of gold. *Philosophical Magazine*, *18*(152), 377–414. https://doi.org/10.1080/14786436808227358

Toledo-Redondo, S., André, M., Aunai, N., Chappell, C. R., Dargent, J., Fuselier, S. A., et al. (2021). Impacts of ionospheric ions on magnetic reconnection and earth's magnetosphere dynamics. *Reviews of Geophysics*, *59*(3), e2020RG000707. https://doi.org/10.1029/2020RG000707

Tucker, O. J., Farrell, W. M., Killen, R. M., & Hurley, D. M. (2019). Solar wind implantation into the lunar regolith: Monte Carlo simulations of H retention in a surface with defects and the H2 exosphere. *Journal of Geophysical Research: Planets*, *124*(2), 278–293. https://doi.org/10.1029/2018JE005805

Verani, S., Barbieri, C., Benn, C., & Cremonese, G. (1998). Possible detection of meteor stream effects on the lunar sodium atmosphere. *Planetary and Space Science*, *46*(8), 1003–1006. https://doi.org/10.1016/S0032-0633(98)00024-5

Wang, X.-D., Zong, Q.-G., Wang, J.-S., Cui, J., Rème, H., Dandouras, I., et al. (2011). Detection of m/q = 2 pickup ions in the plasma environment of the moon: The trace of exospheric h2+. *Geophysical Research Letters*, *38*(14). https://doi.org/10.1029/2011GL047488

Wilson, J. K., Baumgardner, J., & Mendillo, M. (2003). The outer limits of the lunar sodium exosphere. *Geophysical Research Letters*, *30*(12). https://doi.org/10.1029/2003GL017443

Wilson, J. K., Mendillo, M., & Spence, H. E. (2006). Magnetospheric influence on the moon's exosphere. *Journal of Geophysical Research*, *111*(A7). https://doi.org/10.1029/2005JA011364

Wurz, P., Fatemi, S., Galli, A., Halekas, J., Harada, Y., Jäggi, N., et al. (2022). Particles and photons as drivers for particle release from the surfaces of the moon and mercury. *Space Science Reviews*, *218*(3), 10. https://doi.org/10.1007/s11214-022-00875-6

Wurz, P., Rohner, U., Whitby, J., Kolb, C., Lammer, H., Dobnikar, P., & Martín-Fernández, J. (2007). The lunar exosphere: The sputtering contribution. *Icarus*, *191*(2), 486–496. https://doi.org/10.1016/j.icarus.2007.04.034

Yakshinskiy, B., & Madey, T. (1999). Photon-stimulated desorption as a substantial source of sodium in the lunar atmosphere. *Nature*, *400*(6745), 642–644. https://doi.org/10.1038/23204

Yakshinskiy, B. V., & Madey, T. E. (2004). Photon-stimulated desorption of na from a lunar sample: Temperature-dependent effects. *Icarus*, *168*(1), 53–59. https://doi.org/10.1016/j.icarus.2003.12.007

Yamauchi, M., Christon, S., Dandouras, I., Haaland, S., Kastinen, D., Kistler, L. M., et al. (2024). Heavy molecular and metallic ions in the magnetosphere. *Space Science Reviews*, *220*(8), 82. https://doi.org/10.1007/s11214-024-01114-w

Yau, A. W., Whalen, B. A., Goodenough, C., Sagawa, E., & Mukai, T. (1993). EXOS D (Akebono) observations of molecular NO(+) and N2(+) upflowing ions in the high-altitude auroral ionosphere. *Journal of Geophysical Research (ISSN 0148-0227)*, *98*(A7), 11205–11224. https://doi.org/10.1029/92ja02019

Yokota, S., Tanaka, T., Saito, Y., Asamura, K., Nishino, M. N., Fujimoto, M., et al. (2014). Structure of the ionized lunar sodium and potassium exosphere: Dawn-dusk asymmetry. *Journal of Geophysical Research: Planets*, *119*(4), 798–809. https://doi.org/10.1002/2013JE004529

Yokota, S., Terada, K., Saito, Y., Kato, D., Asamura, K., Nishino, M. N., et al. (2020). Kaguya observation of global emissions of indigenous carbon ions from the moon. *Science Advances*, *6*(19), eaba1050. https://doi.org/10.1126/sciadv.aba1050

Zhou, X.-Z., Angelopoulos, V., Poppe, A. R., & Halekas, J. S. (2013). Artemis observations of lunar pickup ions: Mass constraints on ion species. *Journal of Geophysical Research: Planets*, *118*(9), 1766–1774. https://doi.org/10.1002/jgre.20125